

Mechanism and kinetics of reduction of a FeO-Fe₂O₃-CaO-MgO aluminosilicate melt in a high-CO-activity environment

REID F. COOPER,^{1,*} REBECCA L.A. EVERMAN,² JUSTIN W. HUSTOFT,³ AND SANG-HEON DAN SHIM³

¹Department of Geological Sciences, Brown University, Box 1846, Providence, Rhode Island 02912, U.S.A.

²Materials Science Program, University of Wisconsin-Madison, 1509 University Avenue, Madison, Wisconsin 53706, U.S.A.

³Department of Earth, Atmospheric and Planetary Sciences, Massachusetts Institute of Technology, 77 Massachusetts Avenue, Cambridge, Massachusetts 02139, U.S.A.

ABSTRACT

Droplets of an iron-bearing calcia magnesia aluminosilicate (Fe-CMAS) melt were reacted under distinctly reducing conditions ($f_{O_2} = 2.4 \times 10^{-13}$ and 6.4×10^{-15} atm) at high temperature (~1400 °C) and ambient pressure. The low f_{O_2} environment was maintained by a flowing gas mixture of CO and CO₂, with a high content of CO. Molten metallic iron alloyed with silicon and carbon formed on the surface of the melt; no metal was observed in sample interiors. A color change from brown to pale blue confined to the outer layer of the melt indicated that essentially complete reduction of Fe³⁺ to Fe²⁺ had occurred in this region. Analysis of the reaction kinetics, particularly in comparison to melts of similar polymerization but free of CaO, reveals that the concentration of electron holes has decreased to such an extent that ionic transport in the melt is significantly slowed and the diffusion of CO as a neutral species becomes dominant and rate-limiting: molecular CO, initially incorporated into the melt as a physically dissolved species, subsequently reacts to form chemically dissolved (bonded into the melt structure) CO₃²⁻ anions, consuming electron holes in the process. The chemical diffusion coefficient for CO in the reduced melt at 1400 °C is estimated as $D_{CO} \approx 4 \times 10^{-4}$ cm²/s, consistent with that of other, similarly sized molecular species (e.g., H₂ and H₂O) for similarly polymerized melts, as reported by other investigators. Upon quenching, the droplet acts as a closed system. Internal redox couples see the reduction of the carbonate so as to form bubbles of CO, the composition of which are confirmed with Raman spectroscopy. The open-system reduction and closed-system quenching dynamics are analyzed following an Ellingham-diagram approach.

Keywords: Redox, silicate melts, carbon, diffusion, reactions, kinetics

INTRODUCTION

Reduction-to-metal of the more-noble components of a multicomponent silicate melt, e.g., the NiO and FeO components to a (Ni,Fe) alloy, is an important part of the evolution of some chondrules and, too, of the differentiation of the terrestrial planets (e.g., King 1983; Wasson 1985; Lee et al. 1992; Kong and Palme 1999; Libourel et al. 2006). We have studied the kinetics of such reactions and their effects on the texture of a reacted-and-quenched melt. In this reaction, which we describe as “hard” reduction [because, thermodynamically, the chemical-potential difference should change the phase equilibrium from one of a homogeneous melt (hyperliquidus) to one where either the liquid is evolved to sub-liquidus conditions (i.e., precipitation of crystalline metal) or to the formation of a metallic-ionic/covalent liquid emulsion] the kinetic path is one that diminishes the chemical potential differences between the melt and its environment most rapidly. Various textures are possible in such redox reactions, and the one displayed by the system is a function not of thermodynamics, but of the kinetic path in that the texture is a “dissipative structure” in the sense articulated in non-equilibrium thermodynamics (e.g., Kondepudi and Prigogine 1998).

One texture that becomes feasible in a multicomponent system is an “internal” redox reaction, which incorporates two “half reactions” at a minimum [there can be more depending on the system and the difference in oxygen chemical potential involved (e.g., Cooper et al. 1996)] with one occurring at an internal interface that migrates into the material and one occurring at the free surface. Between the two reaction interfaces lies a region of chemical diffusion. There is often chemical diffusion at greater depth than the internal interface, associated with this reaction, as well. This type of internal redox reaction was detailed for crystalline oxide solid solutions by Schmalzried (1983, 1984), an analysis founded on the seminal work of Wagner (1959) on the oxidation of multicomponent metal solutions (alloys).

We have demonstrated that a cation-diffusion-dominated (and rate-limited) internal reaction occurs for the hard reduction of a FeO-bearing magnesium aluminosilicate (Fe-MAS) melt reacted under conditions allowing no convective mixing (Everman and Cooper 2003). The melt, which had a nominal MgO-Al₂O₃-SiO₂ content along the enstatite-cordierite-liquid cotectic with ~20% of the Mg²⁺ replaced with Fe^{2+,3+} and which was reacted at temperatures in the range $1300 \leq T$ (°C) ≤ 1400 and in a controlled oxygen fugacity (f_{O_2}) environment (mixed/ reacted CO+CO₂; f_{O_2} approximately three orders of magnitude below the iron-wüstite buffer, i.e., “IW-3”), developed a reaction texture that included

* E-mail: Reid_Cooper@brown.edu

some uniformly dispersed (micrometer-scale) single crystals of α -Fe (body-centered cubic) on the melt (glass) free surface and, internally, nanometer-scale crystals of α -Fe in a matrix of all-but-fully FeO-depleted magnesium aluminosilicate melt (glass), with the internal reaction terminating at a specific depth—an internal interface separating Fe^{2+} -bearing melt from Fe^{2+} -free melt. The melt (glass) matrix was significantly enriched in silica, due primarily to the loss of FeO. Kinetics analysis indicated that the dynamics were consistent only with the reaction being rate-limited by the “inward” chemical diffusion of the divalent, network-modifying cations. The aluminosilicate network acts essentially as a (relatively) rigid framework for the diffusion. Morphologically, the internal iron nanoparticles were arrayed in a “string-of-pearls” morphology, highly suggestive of the applicability to this melt of the modified random network (MRN) model (e.g., Greaves 1985), in which the network-modifying oxides organize into percolative channels.

An internal reduction reaction in a melt that is rate-limited by diffusion proceeds by a limited number of parallel (independent) kinetic mechanisms, the number affected by the thermodynamic conditions. One of these mechanisms will proceed the “fastest,” that is, it will provide the greatest Gibbs energy change per diffusive step, and so dominate the kinetic response and “set” the texture. Three possible mechanisms for an iron oxide-bearing, alkaline earth silicate composition subjected to a persistent reduction potential created by the mixing and reacting of CO and CO_2 gases are illustrated in Figure 1. A survey of the chemical diffusion literature for melts suggests that these are the most probable mechanisms (cf. Cook and Cooper 2000). Mode I is rate-limited by the diffusion of a neutral gas species, here noted as molecular CO for its reduction potential, its small size and its domination of the external environment setting the low f_{O_2} . Modes II and III involve the diffusion of O^{2-} anions and network-modifying divalent cations (M^{2+}), respectively. These ion fluxes demand charge-compensating complementary fluxes, which are provided by electron holes [h^* , holes are the dominant mobile electronic species in $\text{Fe}^{2+,3+}$ -bearing silicate melts]. Basaltic glass, for example, has been proven to be an h^* conductor (Jurado-Egea et al. 1987), while basaltic melts are perhaps better understood as mixed ionic/ h^* conductors (Pommier et al. 2008; Cooper et al. 1996). In Modes II and III, conditions where the concentration of h^* is nearly zero would see the reaction rate-limited by the electronic conductivity, i.e., by the flux of h^* rather than that of the ions. Each of the modes has an internal reaction texture and involves a free-surface reaction (at ξ') and an internal redox-couple reaction (at internal interface ξ''). The free-surface reaction is in the form of either a redox couple [Modes II and III (e.g., Cook and Cooper 2000)] or a dissolution reaction, Mode I). The dominant reaction mode is best predicted, to first order, by consideration of the transport coefficient, that is, the product of species mobility (diffusion coefficient, D_i , where the subscript i defines the species of interest) and species concentration (c_i) within the reacted material. For example, Mode III, which is the dominant mechanism for the reduction of the Fe-MAS melt described previously, occurs because in the reduced melt $c_{h^*}D_{h^*} \gg c_{M^{2+}}D_{M^{2+}} \gg c_{\text{O}^{2-}}D_{\text{O}^{2-}}$ as well as $\gg c_{\text{CO}}D_{\text{CO}}$ or $c_{\text{O}_2}D_{\text{O}_2}$. Kinetic domination by Mode I, then, would require that the transport coefficient for CO molecules in the reduced melt be notably

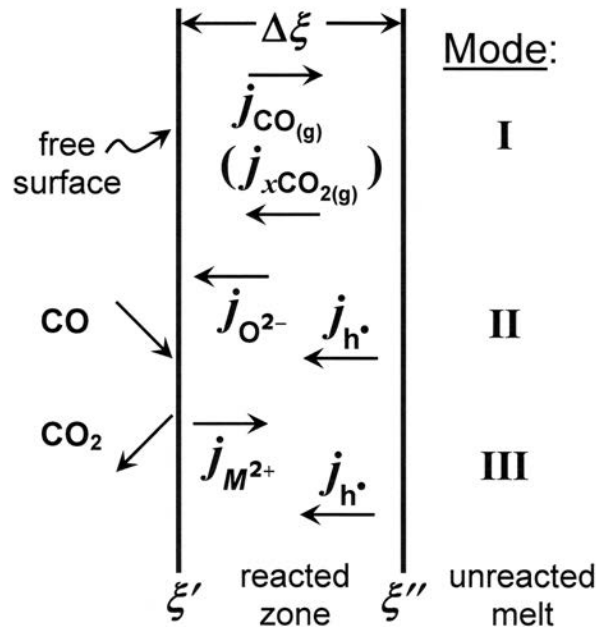


FIGURE 1. Schematic illustration of possible diffusive transport mechanisms for a diffusion-limited internal reduction reaction in an $\text{Fe}^{2+,3+}$ -bearing, alkaline earth aluminosilicate melt where electron holes, h^* , are the primary electronic defect and the low oxygen fugacity external to the melt is created by the dynamic reaction of a mixed CO-CO₂ buffer. Mode I is dominated by the diffusion (flux, j) of molecular CO, Mode II by the diffusion of O^{2-} charge-balanced by a concurrent flux of h^* , and Mode III by the divalent network-modifying cations (M^{2+}) charge-balanced by a counterflux of h^* . The internal (partial) reaction (at ξ'') will involve (at least) a molecular structural change in the melt; it can also involve the precipitation of metal. At the free surface, ξ' , the partial reaction in Mode I involves the physical solution of molecular CO, while that for Modes II and III involve a redox couple in which O^{2-} is chemically ablated from the melt as CO is transformed to CO_2 . The “outward” flux of CO_2 shown in parentheses in Mode I acknowledges the possibility of exceeding the chemical solubility limit for $(\text{CO}_3)^{2-}$ at ξ'' .

greater than those for the network modifying cations, the electron holes or any ionic or atomic oxygen.

Quantifying diffusion-limited redox reactions in melts is a more difficult problem than in the crystalline state. Valence-state change of component ions effects change in the molecular structure of the melt and with it changes in properties such as density, ionic/atomic mobility, gas permeability, electronic conductivity, viscosity, etc. For example, the MRN model should fail when the summed partial molar volumes of modifier-oxides drops below some threshold level (cf. Zallen 1983; Smith and Cooper 2000); this would affect significantly the rate of a diffusion-limited reaction. We attempted similar reduction experiments to those described above on remelted tholeiitic flood basalt and found the response to be quite complicated (we describe qualitatively the results herein). Consequently, we increased the complication of our system for these experiments (compared to the Fe-MAS experiments) solely by the addition of CaO, a network-modifying oxide of significantly greater partial molar volume than MgO or FeO [factors ~ 1.5 and ~ 1.3 , respectively (Lange and Carmichael 1987)] and one known to affect changes in reaction texture and

kinetics during melt and glass oxidation (Smith and Cooper 2000). The higher partial molar volume of CaO may lead to a more open structure and may thereby increase the diffusivity and/or solubility of a gas species in the melt, enabling it to play potentially a more significant role in the reduction reaction. This may favor Mode I over Modes II and III as the predominant reduction mechanism. If Mode I is accessed, the reaction becomes one not only of reduction in a potential gradient of oxygen, but also of the solution formation in a chemical potential gradient of carbon. In this case, the experiments address the petrological problems associated with carbon valence and solubility and its effect on local redox reaction(s) within the silicate melt and, thus, lose their impact on addressing, e.g., the metal-silicate textures seen in primitive chondrules.

EXPERIMENTAL METHODS

Material for the melt reduction experiments was a specially prepared, Fe^{2+,3+}-doped, CaO-MgO aluminosilicate glass (Fe-CMAS). The batch was designed to produce a glass with nominally equal parts (~10 mol%) each of FeO, CaO, and MgO. The exact composition was analyzed using X-ray fluorescence spectroscopy and is presented in Table 1 (compared to the CaO-free, Fe-MAS composition studied previously). The ratio of ferrous to ferric iron in the initial Fe-CMAS material (Fe²⁺/Fe³⁺ = 1.32) was determined by wet chemical analysis. A calculation following the CIPW protocol results in quartz, anorthite, and two pyroxenes being the major normative minerals with minor magnetite. This corresponds to a typical tholeiitic basalt composition with slightly elevated levels of silica and significantly less (here, none) alkalis compared to a natural basalt. To first order, the trace MnO and TiO₂ contents and the potential for heterovalency in silicon notwithstanding, the composition contains but one heterovalent cation species, iron. Further, previous oxidation experiments on glass specimens of this composition can perhaps provide a basis for understanding the kinetic mechanisms in the present study (Smith and Cooper 2000).

The starting glass was created using high-purity production-grade MgO, Al₂O₃, and SiO₂, and analytical-reagent-grade CaO and FeC₂O₄·2H₂O powders. A ~2 kg batch was prepared by measuring each component to an accuracy of ±0.1 g. The batch was placed in an iron-soaked platinum crucible (to minimize iron loss from the melt) (Grove 1981; Kessel et al. 2001) and melted in air at 1550 °C for 8 h. During the melting phase, at high temperature, CO (released from the ferrous iron oxalate) bubbled through the melt. This technique allows for the retention of ferrous iron instead of the ferric iron that is in equilibrium with the furnace conditions. The melt was poured into a patty, broken into coarse pieces, and remelted under the same conditions for another 8 h. The melt was poured into a 15 × 15 × 4 cm patty and annealed at 700 °C in air for 24 h to remove residual stresses.

TABLE 1. Initial compositions of Fe-CMAS and Fe-MAS glass melts used for reduction experiments

Oxide	Fe-CMAS		Fe-MAS*	
	wt%†	mol%‡	wt%†	mol%‡
SiO ₂	59.00	62.97	59.24	59.24
TiO ₂	0.01	0.01	0.03	0.02
Al ₂ O ₃	13.00	8.18	15.49	9.13
Fe ₂ O ₃ ‡	6.30	2.53	2.05	0.77
FeO‡	7.50	6.69	5.63	4.71
MgO	6.02	9.58	17.40	25.94
CaO	8.77	10.03	0.13	0.14
MnO	0.02	0.02	0.01	0.01
Na ₂ O	—	—	0.04	0.04
Totals	100.62	100.00	100.02	100.00
Fe ³⁺ /ΣFe	0.430		0.247	
NBO/T	0.370		0.530	
V _{m,1673K} **	24.7 cm ³ /mol		23.3 cm ³ /mol	

* Everman and Cooper (2003).

† X-ray fluorescence: XRAL Laboratories, Don Mills, Ontario, Canada.

‡ Wet chemical analysis: Corning, Inc., Corning, New York.

§ Calculated from oxide wt% normalized to 100%.

|| Non-bridging O²⁻ normalized by tetrahedral cations (atomic fraction) (Mysen 1988).

** Molar volume at 1400 °C, calculated using model of Lange and Carmichael (1987).

The cooled patty was black in color indicating the presence of some ferric iron (consistent with the data in Table 1) and free of "cord" (i.e., visible chemical composition gradients).

The reduction experiments were conducted in a vertical tube furnace by suspending a 2–3 mm cube cut from the interior of the glass patty in a Pt (99.99% metals basis) wire cage. The experimental conditions are summarized in Table 2. The samples were reacted at temperatures ranging from 1368 to 1407 °C; at these temperatures the melt is above its liquidus while pure metallic iron is below its melting point. A type C (W-5%Re/W-26%Re) thermocouple, placed less than a centimeter away from the sample, monitored the temperature. Temperature control had a precision of ±0.5 °C. The silicate melt was held in the wire cage by surface tension.

The oxygen fugacity in the furnace was controlled by a flowing gas mixture of CO₂ and CO. The experiments were done in two *f*_{O₂} regimes: one corresponding to an equilibrium *f*_{O₂} approximately three orders of magnitude below the iron-wüstite buffer (Myers and Eugster 1983) (IW-3; actual *f*_{O₂} ≈ 2.4 × 10⁻¹³ atm at 1370 °C) and the other to four and a half orders of magnitude below IW (IW-4.5; actual *f*_{O₂} ≈ 6.4 × 10⁻¹⁵ atm at 1400 °C). The gases were mixed at a CO₂:CO ratio of ~1:240 for the IW-3 runs with a total gas flow rate of 270 cm³/min and ~1:750 for the IW-4.5 runs with a total gas flow rate of 200 cm³/min. The *f*_{O₂} was monitored with a yttria-stabilized zirconia oxygen sensor (Ceramic Oxide Fabricators, Australia) that was located inside the furnace tube at the same level as the sample. The readings were adjusted for the non-Nernstian behavior at extremely reducing conditions according to the method outlined by Mendybaev et al. (1998).

The sample cage was suspended between two molybdenum wires by a tungsten filament. When the selected reaction time was completed, the sample was dropped out of the hot zone of the furnace by applying a voltage across the Mo wires and so burning-up the W filament. This procedure produced nearly instantaneous quenching. The resulting samples were stored in a desiccator to slow any further reaction with the ambient air at room temperature.

The reacted and quenched droplets were analyzed using both light and electron microscopies. The surface of the droplets was investigated using reflected light microscopy, backscattered electron imaging (BSE) in the scanning electron microscope (SEM), and energy dispersive X-ray spectroscopy (EDS; performed in the SEM) to evaluate the composition, size, and distribution of metallic phases on the surface. The droplets were then cross-sectioned and examined in transmitted light microscopy, transmission electron microscopy (TEM), and EDS (performed in a scanning-TEM). The cross-sections were used to analyze the reaction kinetics (light transmittance in optical microscopy, characterized digitally) and to discern the presence (or absence) of crystalline phases (TEM) within the reacted portion of the melt.

Raman spectroscopy was applied to some of the IW-4.5 specimens, to characterize the contents of fine bubbles that resulted from the processing (i.e., the reaction and quenching) of the melt droplets. The analytical conditions employed included excitation by the 514.5 nm line of an Ar/Kr mixed-ion laser at 10 mW power at the specimen and a beam diameter of 10 μm; the spectral resolution was ~2 cm⁻¹ as constrained by a diffraction grating of 600 grooves mm⁻¹ and 45 cm⁻¹ min⁻¹ scan speed.

RESULTS

Visual inspection and low-magnification optical microscopy reveal two features of the reacted and quenched Fe-CMAS droplets: (1) the droplet exterior typically has spherical precipitates

TABLE 2. Fe-CMAS—Experimental conditions and reaction-extent results

<i>f</i> _{O₂} regime	Specimen no.	<i>T</i> (°C)	<i>f</i> _{O₂} (atm)	<i>t</i> (s)	Δξ (cm)
IW-3	RE041102	1369	2.60 × 10 ⁻¹³	1790	9.29 × 10 ⁻³
	RE080802	1372	2.30 × 10 ⁻¹³	2460	1.03 × 10 ⁻²
	RE100302	1373	3.10 × 10 ⁻¹³	3520	1.25 × 10 ⁻²
	RE081302	1368	2.00 × 10 ⁻¹³	4140	1.72 × 10 ⁻²
	RE090902	1369	2.00 × 10 ⁻¹³	7140	1.81 × 10 ⁻²
	average	1370.2	2.4 × 10 ⁻¹³		
IW-4.5	RE031203	1398	—*	850	
	RE030803	1401	8.00 × 10 ⁻¹⁵	1670	
	RE030703	1400	8.60 × 10 ⁻¹⁵	2580	
	RE030303	1403	7.20 × 10 ⁻¹⁵	3600	
	RE0022703	1407	3.50 × 10 ⁻¹⁵	7040	
	average	1401.8	6.43 × 10 ⁻¹⁵		

* *f*_{O₂} meter inoperative: CO:CO₂ ratio same as in other IW-4.5 runs.

dispersed over the surface (shown more dramatically in the BSE/SEM image presented as Fig. 2), and (2) for the IW-4.5 specimens only, fine, dispersed bubbles are present (Fig. 3).

The precipitates, which demonstrate metallic reflectivity optically, range in size from $\sim 2 \mu\text{m}$ diameter spheres to $\sim 100 \mu\text{m}$ globules. The larger globular precipitates tend to be spatially associated with the wire cages. As seen in Figure 2 (1407 °C; IW-4.5; 7040 s), the distance separating the smaller precipitates is notably less than that separating the larger ones. The precipitates make up 8.8% of the surface area and the volume of the particles at the surface per μm^2 of surface area is $\sim 0.50 \mu\text{m}^3/\mu\text{m}^2$. In terms of the areal density and normalized volume of the surface precipitates, there were no systematic differences between samples reacted at the IW-3 conditions vs. the IW-4.5 conditions. EDS was used to verify the composition of the crystals. They are predominately iron but contain approximately 2–3 at% Si (the higher Si content in the IW-4.5 specimens). Carbon may also be present in the precipitates, but quantitative measurements are unavailable because the samples were carbon-coated to cut down on the sample charging in the electron microscope. The spherical morphology of the iron indicates that the precipitates were at least partially molten, and probably fully molten. The result suggests that carbon concentration in the precipitates is significant. For example, an iron-3 at% silicon alloy would be at its liquidus at 1400 °C only if it contained a minimum of 1 wt% or 4.4 at% carbon (e.g., Raghavan 1986).

When the reacted and quenched silicate droplets are sliced in half and viewed in transmitted light, the reacted zone is clearly visible with a distinct color change from dark brown in the interior to nearly clear or very pale blue on the rim as shown in the cross-sectional view (in grayscale) in Figure 4a (inset) for an IW-3 reaction. Samples run under the extremely reducing conditions (IW-4.5) show the same color change in addition to the bubbles mentioned above (Fig. 5). These droplets contain

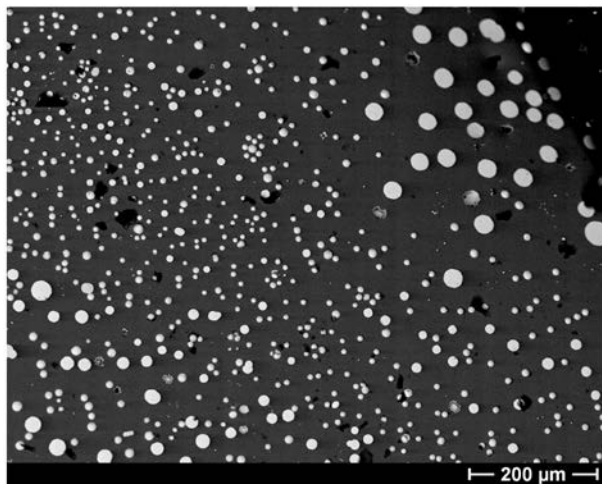


FIGURE 2. BSE/SEM image of the free surface of a Fe-CMAS melt droplet reacted at 1407 °C and IW-4.5 for 7040 s (Specimen RE022703). EDS analysis of surface precipitates indicate that they are an iron plus ~ 2.7 at% silicon alloy. The spherical morphology of the precipitates indicates that they were molten (or perhaps partially molten) under the conditions of the reaction. This means that the alloy must contain, additionally, ≥ 4 at% carbon.

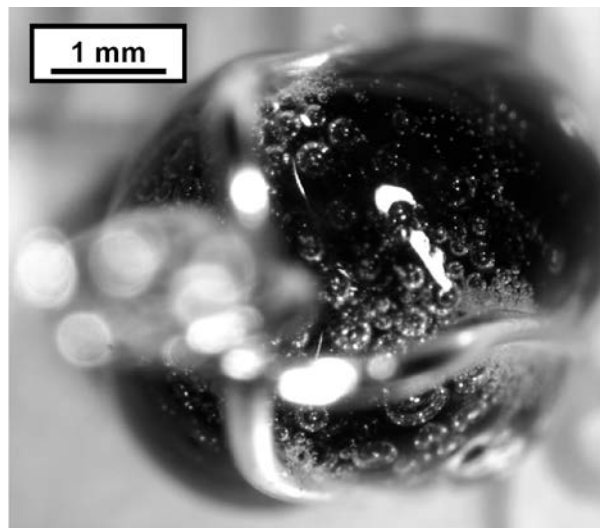


FIGURE 3. Binocular microscope image of the top half of a Fe-CMAS melt droplet reacted at 1401 °C and IW-4.5 for 1670 s (Specimen RE030803). The remnant of the Pt-wire cage is visible but out of focus. Sub-surface bubbles are evident, with diameters of up to 500 μm (although most are smaller than 250 μm , ranging to $\sim 1 \mu\text{m}$); the bubbles exist only in a shell around the droplet, that is, their presence terminates at a specific internal distance. There is a higher density of bubbles near the Pt wires; Raman analyses were done of bubbles both near and far away from the wires. The very finest bright specks seen in the upper-right quadrant of the droplet image are the larger of the alloy precipitates shown in higher magnification in Figure 2.

bubbles throughout the volume of the quenched specimens from reaction times in excess of 1800 s. Bubbles were never seen in the IW-3 samples, even after a reaction time of 2 h (7200 s).

As the iron ions are reduced, the sample transitions from a combination of ferric and ferrous iron to predominately ferrous iron, with the result being the transition in color described above (e.g., Zarzycki 1991; Weyl 1951; Schofield et al. 1995). This phenomenon is examined in the Discussion. This color change, thus, clearly delineates the location of an internal reaction front. Figure 4b shows the transmittance of light along the line segment A-A' in the quenched Fe-CMAS droplet shown in Figure 4a. The inflection point in the transmittance was used as the location of the internal reaction front for the purposes of evaluating the kinetics of the reaction. Because of the influence of the Pt wires on the progress of the reaction (as seen by the lack of color change by those wires), the internal reaction front depth ($\Delta\xi$) was measured as far removed from the wires as possible. The kinetic analysis for five experiments performed at 1370 ± 2 °C at IW-3 is presented in Figure 6 (the data listed in Table 2), in which the square of the distance from free surface ξ' to internal interface (i.e., transmittance inflection) $\xi'' - (\Delta\xi)^2$ —is plotted against time. The linear relationship so discovered is proof that the reduction reaction is rate-limited by chemical diffusion. For comparison, the kinetic analysis of Fe-MAS melt reacted at 1385 °C (Everman and Cooper 2003) is plotted on the same figure. The Fe-MAS melt has a similar polymerization to the Fe-CMAS melt as calculated from the atomic ratio of non-bridging O^{2-} (that is, O^{2-} bonded to two network-forming cations)

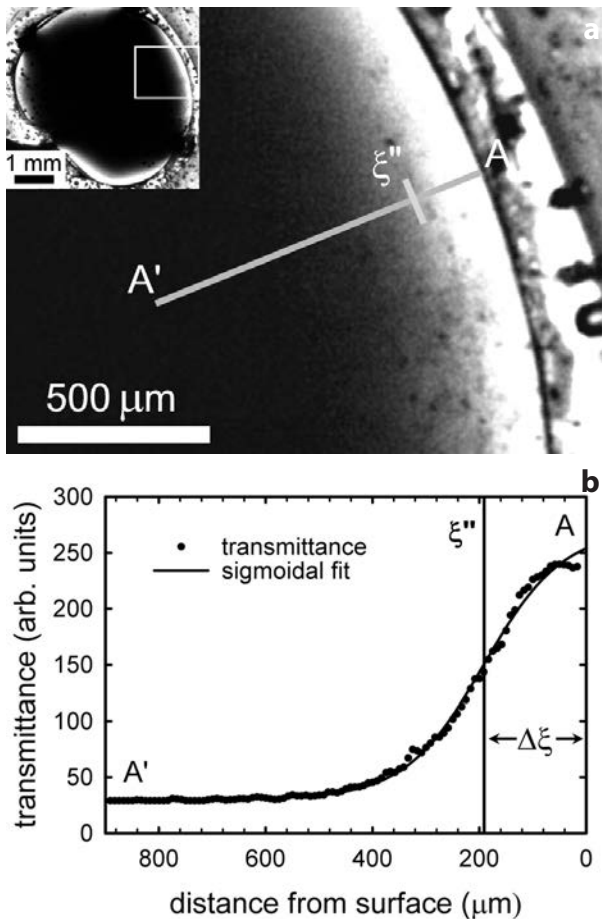


FIGURE 4. Cross-sectional views of a reacted and quenched Fe-CMAS melt droplet (1368 °C; IW-3; 4140 s—Specimen RE081302). (a) Transmitted light micrographs: the inset figure shows the full cross-section of the sample. The lighter color clearly distinguishes the reaction zone in the sample. The dark (unreacted) color in the center also approaches the surface where the Pt wires were holding the sample. Kinetic data were collected from areas as far from the wires as possible to avoid any effects due to the presence of the wire. The main image is a close-up view of the boxed area in the inset showing the traverse line (A–A′) from which the kinetic data were collected. (b) Light transmittance as a function of distance along the line segment A–A′. The inflection point was used as the nominal location of the internal reaction for the purposes of the kinetic analysis.

to tetrahedrally coordinated, network-former cations—NBO/T (e.g., Mysen 1988)—where Fe-MAS has a NBO/T = 0.53 and Fe-CMAS a NBO/T = 0.37 (Table 1). In the comparison of the reaction kinetics, one sees that the effective parabolic reaction rate constant, k' , is almost two orders of magnitude smaller for the Fe-CMAS composition for similar conditions of temperature and oxygen activity potentials. Kinetic analysis of the IW-4.5 samples was not attempted due to the uncertainty in $\Delta\xi$ because of the presence of the bubbles.

Careful analysis by conventional TEM demonstrated that the reduced region of the Fe-CMAS, IW-3 quenched droplets (the region between ξ' and ξ'') was a homogeneous glass, that is, it contained no second phase [metallic or otherwise, crystalline

or amorphous (i.e., an emulsion did not form to a resolution of ~ 1 nm)], a result in stark contrast to α -Fe precipitates found in the reduced region of the Fe-MAS droplets. Indeed, it was the lack of metal precipitates in the reacted zone of the IW-3 samples that prompted the IW-4.5 experiments, assuming that the reason for this lack was a decreased activity of FeO in the Fe-CMAS composition due specifically to the CaO component. However, at IW-4.5 conditions, there were still no second phases (metallic or otherwise) interior to the reacted silicate melt, even at nanometer scale.

Raman spectroscopy of the bubbles (Fig. 7) revealed a distinct difference in the contents, depending on whether or not the bubble was in contact with Pt wire. When not near the Pt wires, analyzed bubbles revealed two peaks, one centered at 2140 cm^{-1} and one centered at 1865 cm^{-1} (Fig. 7a). Comparison to references (Wopenka and Pasteris 1987; Speight 2005) indicate that the former is associated with molecular CO and the latter with CO-O carbonyl bonds. Bubbles in contact with platinum, however, show broad peaks centered at 1375 and 1600 cm^{-1} (Fig. 7b), consistent with molecular CO_2 and with disordered graphite, respectively (Wopenka and Pasteris 1987; Ferrari and Robertson 2000).

DISCUSSION

An understanding of the dynamics of the reduction reaction in the Fe-CMAS melt requires the integration of five observations and their comparison to the reduction dynamics in the Fe-MAS melt described previously (Everman and Cooper 2003). The five observations are: (1) the color change from the original brown to a pale blue in the reduced material (Figs. 4 and 5); (2) the distinctly slower kinetics for the reduction of the Fe-CMAS melt compared to the Fe-MAS melt (Fig. 6); (3) the presence of molten iron that is alloyed with silicon and carbon

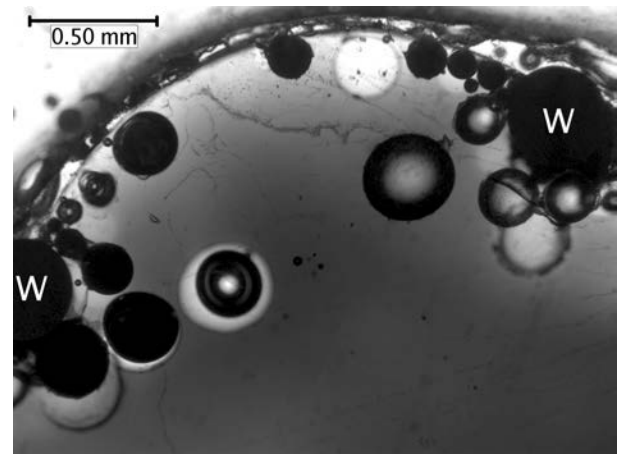


FIGURE 5. Cross-sectional, transmitted-light micrograph a Fe-CMAS droplet reacted at 1401 °C and IW-4.5 for 1670 s (Specimen RE030803; Fig. 3). The “W” symbol denotes the cross-section of the Pt wires. Bubbles are found near the free surface of the droplet (although they are more prevalent near the Pt wires). Their presence terminates at a specific depth (~ 0.8 mm). Loss of color near the free surface of the quenched specimens remains evident. Color loss in the surface region farthest removed from the wires is correlated with the bubbles.

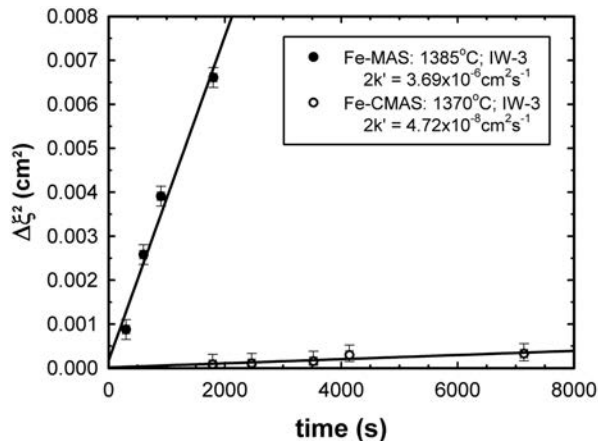


FIGURE 6. Reaction distance squared ($\Delta\xi^2$) as a function of time for Fe-CMAS and Fe-MAS (Everman and Cooper 2003) compositions. The linear relationship in this plot (i.e., parabolic kinetics, $\Delta\xi^2 = 2k't$) indicates that the reduction reactions are rate-limited by chemical diffusion; k' is the parabolic reaction-rate constant. For nominally similar thermodynamic conditions of T and f_{O_2} , k' for the Fe-CMAS melt is two orders of magnitude smaller than that for the Fe-MAS melt.

at the surface of the Fe-CMAS specimens (Fig. 2); (4) the lack of any metallic precipitates inside the reacted Fe-CMAS melt despite the presence of metallic iron at the surface; and (5) the presence of bubbles in Fe-CMAS samples reacted at the lower (IW-4.5) f_{O_2} conditions, their presence being limited to a finite depth in specimens reacted for short reaction times (Fig. 5), and their containing essentially pure CO_(g) in regions of the specimen removed from the Pt-wire cage (Fig. 7a). We pursue these observations in turn.

Color in Fe^{2+,3+}-bearing silicates

In all of the present experiments (as well as in the Fe-MAS melts studied previously), a distinct color change was visible from the original dark brown to a pale blue. The color produced by Fe^{2+,3+}-bearing aluminosilicate compositions varies considerably depending on the valence-state partitioning and coordination of the iron cations (Weyl 1951), which are influenced by the bulk composition, the oxygen activity, and the total Fe²⁺-Fe³⁺ content (e.g., Mysen et al. 1985). In amorphous silicates, ferrous iron ions typically absorb in the infrared band, and the absorption extends into the visible region of the spectrum causing a blue color. Ferric iron absorption depends on its coordination, with tetrahedral Fe³⁺ absorbing strongly in the blue region resulting in a brown color, while ferric iron in octahedral coordination is colorless (although in crystalline silicates, octahedral ferric iron gives the crystal a red color). It is also possible for ferrous and ferric ions to associate with each other and form a chromophore group, which absorbs at all transitions, and, depending on the accumulation/concentration of these groups, the resulting color ranges from blue to gray to black (Weyl 1951).

The original color (i.e., in sections <1 mm thick) of the Fe-CMAS glass was a dark brown, indicative of the presence of tetrahedrally coordinated ferric iron and perhaps some concentration of the Fe²⁺/Fe³⁺ chromophore groups. As the melt

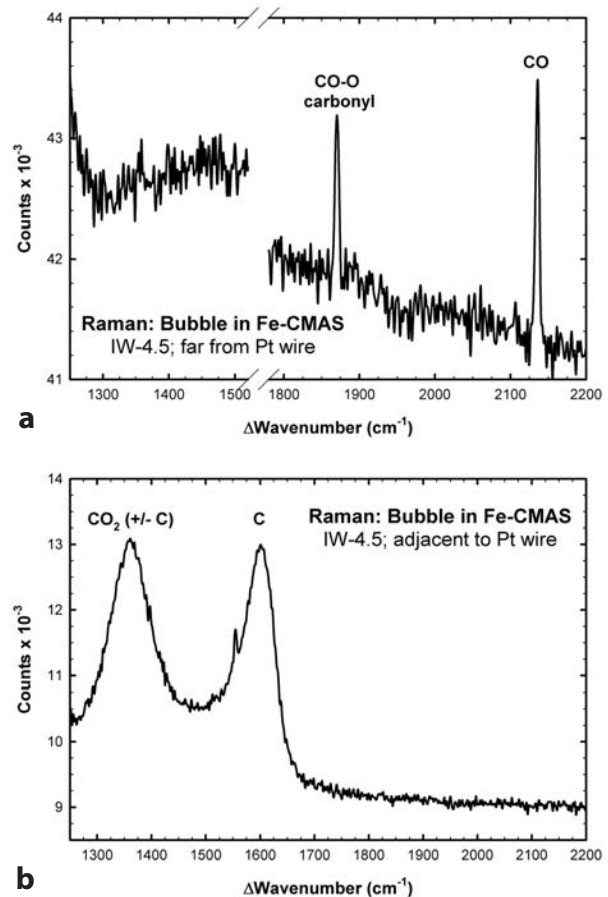


FIGURE 7. Raman spectra of bubbles in Fe-CMAS droplet processed at 1401 °C and IW-4.5 for 1670 s (Specimen RE030803; cf. Fig. 3). (a) Bubble far from Pt wire cage: peaks correlate to CO and a CO-O carbonyl; no peaks in the wavenumbers associated with CO₂. (b) Bubble adjacent to Pt wire: a mixture of CO₂ and condensed carbon (disordered graphite) is indicated; peaks associated with CO and carbonyl are absent.

was reduced, it changed to a pale blue color, which indicates (at minimum) an increased ratio of ferrous to ferric iron, but is more likely the product of the nearly complete reduction of tetrahedral ferric iron to ferrous iron (Schofield et al. 1995). The presence/absence of octahedrally coordinated ferric iron cannot be deduced from the color change.

Analysis of reaction kinetics and dominant kinetic modes

Experiments on the oxidation response of glasses of the Fe-CMAS composition (annealed to supercooled-liquid structure) demonstrated a dynamic involving the diffusion of network-modifying divalent cations to the free surface of the samples, charge-balanced by a counterflux of electron holes (Smith and Cooper 2000). This dynamic is essentially a mirror image of the Mode III kinetic path shown in Figure 1 (cf. Cook and Cooper 2000). The Mode III mechanism also characterizes the reduction reaction in the Fe-MAS melt (Everman and Cooper 2003). Thus, it is reasonable to evaluate the Mode III kinetics for the reduction of the Fe-CMAS melt. The reduction reaction at IW-3 (Figs. 4 and 6) shows that the reaction progress is characterized

by parabolic kinetics, indicating that chemical diffusion is the rate-limiting step, specifically,

$$\frac{d(\Delta\xi)}{dt} = \frac{k'}{\Delta\xi}, \text{ or } (\Delta\xi)^2 = 2k't, \quad (1a \text{ and } 1b)$$

where $\Delta\xi$ is the observed reaction thickness (Fig. 4), t is the reaction time, and $2k'$ is the slope of a plot of the reaction distance squared vs. reaction time (Fig. 6). Practically, k' is proportional to the product of a diffusion coefficient and a (normalized to RT , where R is the gas constant and T is temperature) Gibbs energy driving potential ($\Delta_r G$) (e.g., Schmalzried 1981). One can discern this relationship by pursuing the reaction growth rate in terms of the flux(es) involved, i.e., the rate of reaction progress into a material is simultaneously described by

$$\frac{d(\Delta\xi)}{dt} = j_i V_m \lambda \quad (2)$$

where V_m is the molar volume of the melt, λ is a stoichiometric factor representing the amount of melt required to react with 1 mole of diffusant, and j_i is the flux of the rate-limiting species in units of number per area per time. Flux is a convolution of the transport coefficient and the driving force for the diffusion, and is described by Fick's first law, in this case as written for ionic materials [the Fick-Einstein equation (e.g., Schmalzried 1981)]:

$$j_i = \frac{-c_i D_i}{RT} \left(\frac{d\eta_i}{d\xi} \right) = \frac{-c_i D_i}{RT} \left(\frac{d\mu_i}{d\xi} + z_i F \frac{d\phi}{d\xi} \right) \quad (3)$$

where z_i is the charge (valence) of species i , F is the Faraday constant, and $(d\eta_i/d\xi)$ the electrochemical potential gradient that can be separated into its chemical potential ($d\mu_i$) and electrical potential ($d\phi$) contributions. The combination of Equations 1–3 gives an expression for k' :

$$k' = \frac{\lambda V_m c_i D_i d\eta_i}{2RT} = \frac{\lambda V_m c_i D_i (d\mu_i + z_i F d\phi)}{2RT} \quad (4)$$

The three main variables that contribute to the parabolic rate constant are the differences in chemical and electrical potential, the mobility of the rate-limiting diffusant (D_i/RT), and the concentration of the diffusing species. The reader is referred to Everman and Cooper (2003) for details of the analysis. In outline, Mode III is concerned about inward diffusion of divalent cations (i.e., $i \equiv M^{2+}$); the cations diffuse in response to the gradient in the chemical potential of oxygen:

$$j_{M^{2+}} = \frac{+c_{M^{2+}} D_{M^{2+}}}{2RT} \frac{d\mu_{O_2}}{d\xi} \quad (5)$$

Combining Equations 1–5, one can solve for the diffusion coefficient of the divalent cations:

$$D_{M^{2+}} = \frac{RT(\Delta\xi)^2}{\lambda X_{M^{2+}} \Delta t \Delta \mu_{O_2}} = \frac{(\Delta\xi)^2}{\lambda X_{M^{2+}} \Delta t \ln \left(f_{O_2}'' / f_{O_2}' \right)} \quad (6)$$

where f_{O_2}'' is the oxygen fugacity at the internal reaction front ξ'' , f_{O_2}' is the oxygen fugacity at the free surface ξ' , and $X_{M^{2+}}$ is the mole fraction of divalent cations (equal to $c_{M^{2+}} V_m$). $X_{M^{2+}}$ is the sum of the mole fractions of CaO, FeO, and MgO from Table 1, and λ is calculated to be 45.3 based on $X_{Fe_2O_3}$. In this calculation of k' , we assume the internal reaction front occurs at the inflection point in the transmitted light intensity, as shown in Figure 4. The f_{O_2}'' at this internal reaction front cannot be known exactly; we approximate it at $f_{O_2}'' = 2.3 \times 10^{-6}$ atm, a value corresponding to the oxygen fugacity where all ferric iron is converted to ferrous iron as calculated from the fayalite-hematite-quartz (FHQ) reaction equilibrium, adjusted for the activities of these oxide components being less than unity in the melt. [FHQ is based on the speciation approach of the multicomponent silicate solution thermodynamic model MELTS (Ghiorso and Sack 1995)—all Fe²⁺ is accounted for in a fayalite component, all Fe³⁺ is accounted for in a hematite component; we employed MELTS to discern this value of f_{O_2}'' .] Incorporating all these factors into Equation 6, the calculated result is $D_{M^{2+}} = 2.4 \times 10^{-10}$ cm²/s. This value is an order of magnitude slower than the oxygen tracer diffusion coefficient (e.g., Dunn 1982) and three orders of magnitude slower than divalent cation tracer diffusion coefficients (e.g., Cook et al. 1990) in melts of comparable polymerization. Clearly, the assumption of the reaction being rate-limited by the diffusion of divalent cations is unrealistic.

The other mobile species in the Mode III reaction, though, is electron holes. Thus far we have assumed that $c_h D_h \gg c_{M^{2+}} D_{M^{2+}}$ [the “semiconductor condition” (Schmalzried 1981)]. This assumption is generally reasonable because $D_h \gg D_{M^{2+}}$. However, if c_h is small enough, the assumption no longer holds. If the melt is depleted of electron holes, the chemical diffusion of ion species is no longer decoupled (i.e., from the anions or other cations). The result is that the effective diffusion coefficient is no longer that of the divalent cation, but a convolution of the concentration and diffusion coefficients of the primary diffusive species (i.e., h^* and M^{2+}) and in this way the electronic conductivity becomes a factor in the rate constant, slowing down Mode III. The unrealistic value calculated for the diffusion coefficient of divalent cations based on k' demonstrates clearly that the semiconductor condition no longer holds for the reduced melt.

If the concentration of electron holes is decreased such that $c_h D_h < c_{M^{2+}} D_{M^{2+}}$, Mode III may still be the dominant mechanism, just with a slower effective diffusion coefficient. Alternately, the kinetics could be slowed to the point that another mode becomes faster than Mode III. Since both Modes II and III in Figure 1 have ionic fluxes that are charge-balanced by the flux of electron holes, and knowing that $c_{O_2} D_{O_2} < c_{M^{2+}} D_{M^{2+}}$, both from tracer diffusion measurements as well as from oxidation experiments on Fe-CMAS (Smith and Cooper 2000), Mode II will never be the dominant mechanism in this melt. In both cases, if the electrical conductivity of the material is lowered, the reaction mechanism will be shut down due to the build up of voltage across the material. The kinetic analysis shows that Mode III has been shut down, indicating that the electronic conductivity has become limiting, suggesting that another mechanism is occurring—one that consumes electron holes.

Reaction mechanisms and carbon incorporation

At the beginning of an experiment, that is, upon the contact of the melt originally equilibrated at one f_{O_2} with an environment at a significantly different f_{O_2} , all of the kinetic modes are available and operative. There may be only small differences in the kinetics of each of the modes initially, but eventually one of the modes will “win,” subjugating—essentially shutting down—other mechanisms, depending on the molecular structural change of the melt associated with the mechanism. In the case of the reduction of the Fe-CMAS melt, the kinetic analysis above indicates that electron holes must be consumed and the presence of bubbles in the quenched droplets reacted under IW-4.5 conditions suggests that the role of gas species in the external environment has become significant in the reaction. The combination of these factors suggests that the Mode I mechanism has become dominant.

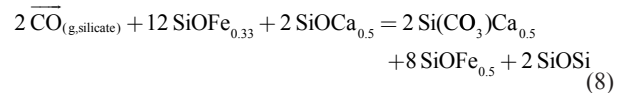
To understand how the consumption of electron holes occurs in Mode I, one must first consider the effects of the difference of chemical potential of carbon between the gaseous environment—which, continually renewed, buffers the system—and the initial melt droplet. Carbon can be incorporated into the melt in several ways. It can be physically dissolved as neutral molecules of CO and/or CO₂ in the “free volume” of the melt (where only weak van der Waal’s interactions occur between the polar carbon oxide molecules and the locally charge neutral but polar units of the silicate melt) (e.g., Doremus 2002) or it can be chemically dissolved in the form of CO₃²⁻ where tetravalent carbon is bonded into the melt structure (e.g., Egger et al. 1979; Fine and Stolper 1985/86; Pawley et al. 1992; Thibault and Holloway 1994; Dixon et al. 1995; Brooker et al. 2001a).¹ The speciation between physically dissolved CO₂ and chemically dissolved CO₃²⁻ (both with C⁴⁺) depends both on the polymerization of the melt and its iron-oxide redox state. In iron-oxide-free melts, less polymerized melts favor incorporation of CO₃²⁻, whereas in Fe^{2+,3+}-bearing melts, carbonate incorporation is favored for melts having Fe³⁺ as a network former. In general, though, CO₃²⁻ is preferentially associated with NBOs and with Ca²⁺, if available (e.g., Brooker et al. 2001a). In basaltic-composition melts, C⁴⁺ is found exclusively in CO₃²⁻ form (e.g., Nowak et al. 2003).

Under the experimental conditions studied here, the activity of CO in the environment is extremely high, the partial pressure of CO being approximately the entire pressure, i.e., $p_{CO} \sim 1$ atm, so there is a significant driving potential for the incorporation of CO into the melt. Once inside the melt, CO can react to form CO₃²⁻, consuming electron holes. Thus, the consumption of electron holes comes about in the same reaction that allows the melt to lessen the chemical potential difference of carbon in the

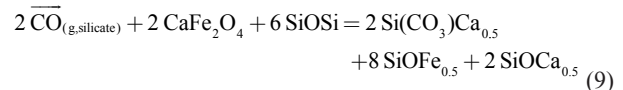
system. The overall reaction involved in reduction Mode I (Fig. 1) is characterized by specific half reactions, at ξ' ,



and at ξ'' ,



where the arrow represents the diffusion of carbon monoxide molecules through the reacted melt to the internal interface (ξ''). Reaction Equation 7 is the physical dissolution of CO into the melt. Reaction Equation 8 describes the chemical dissolution of CO (C²⁺) as carbonate (C⁴⁺); carbon is oxidized by reducing the Fe³⁺. Reaction Equation 8 is written in the polymerization notation of Hess (1980);² electron holes are the equivalent of network-modifying ferric iron, i.e., 3SiOFe_{0.33} (Cook and Cooper 2000). Interpreting Equation 8, for each two molecules of CO_(g, silicate) incorporated as carbonate [2Si(CO₃)Ca_{0.5}], four h^{*} are consumed; network modifying ferrous iron, as well as bridging O²⁻, are products. An alternative reaction in which CO is oxidized and incorporated as carbonate is



where CaFe₂O₄ represents a Ca²⁺ charge-balancing two network-forming Fe³⁺. In the absence of alkali cations, as is the case for the Fe-CMAS composition studied here, Ca²⁺ is the preferred divalent species of those available to charge-balance network-forming ferric iron (Mysen et al. 1985; Hess 1995). This reaction describes the conversion of tetrahedrally coordinated ferric iron into network-modifying ferrous iron, and it must be occurring along with reaction Equation 8 to account for the color change observed in the reacted droplets. These two reactions differ dramatically in their predicted effect on the polymerization of the melt, however. In Equation 8, bridging oxygen are formed, increasing polymerization and viscosity, whereas in Equation 9, bridging oxygen are consumed, decreasing polymerization and viscosity. Viscosity data on ash slags equilibrated in CO:CO₂ gas mixtures indicates that overall the viscosity of Fe-bearing silicate melts decreases as it is reduced (Nowok 1995), a result that is more consistent with Equation 9 than with Equation 8. Of course, the reactions above are coupled by the homogeneous equilibrium

¹There exists no spectroscopic evidence for any chemically dissolved C²⁺ species in multicomponent silicate melts (e.g., Egger et al. 1979), but under extremely reducing conditions it is possible to incorporate carbon in the melt where it is covalently bonded to silicon. This highly reduced form of carbon is seen in silicon oxycarbide glasses (Pantano et al. 1999; cf. Mendybaev et al. 2002), and has only been studied in connection with the four-component Si-C-O-H system. In this regard, dominance of this type of silicon-carbon bonding anticipates f_{O_2} conditions on the order of 10⁻¹⁷ atm at 1400 °C.

²Hess-notation reactions are balanced and describe, in simplified form, how a reaction affects the molecular structure in a melt. The melt components are described in terms of the bonding environment of oxygen anions: each O²⁻ has Pauling bond strengths to cations that sum to 2. For example, SiO_M corresponds to a non-bridging oxygen bonded to a network-modifying divalent cation, so 2SiO_M can represent the cation (e.g., in Eq. 8, 2SiOCa_{0.5} is a network modifying Ca²⁺); similarly, 3SiOFe_{0.33} represents a network-modifier ferric iron. SiOSi is a bridging oxygen connecting two silica tetrahedra.



which describes the balance between network-former and -modifier Fe³⁺; a lowering of the activity (concentration) of either ferric species via a reduction reaction results in the lowering of both. Mössbauer spectroscopy studies on Fe^{2+,3+}-bearing CMAS melts (Mysen et al. 1985) suggest that the Fe-CMAS composition studied here has most Fe³⁺ in the network-former role; the dominance of reaction Equation 9 is so suggested.

In seeking, then, to explain why the incorporation of carbon into the melt did not influence the kinetics of the reduction reaction in the Fe-MAS melt previously studied, which clearly followed Mode III kinetics, we look specifically to the effect of CaO on the chemical and physical solubilities of carbon species in the melt. Ca²⁺ has a direct effect on the solubility of chemically dissolved CO₃²⁻ and an indirect effect on the solubility of physically dissolved CO, effects in part characterized experimentally and corroborated by thermodynamic data. Brooker et al. (2001b) used Fourier-transform infrared spectroscopy to demonstrate that a jadeite-composition melt doped with CaO favors chemically dissolved CO₃²⁻, whereas one doped with an equimolar amount of MgO favors more physically dissolved CO₂. This result is consistent with thermodynamic data/analyses that indicate, while the incorporation of CO₂ into a silicate melt is an endothermic reaction (i.e., chemical solubility increases with temperature), the reference-state reaction Ca₂SiO₄ + CO₂ = CaSiO₃ + CaCO₃ (larnite to wollastonite + calcite) is: (1) significantly less endothermic (by ~60%) than the equivalent reaction of forsterite to enstatite + magnesite, and (2) has approximately equal entropy change (Spera and Bergman 1980; cf. Kubaschewski et al. 1967, Table E). The increased molar volume of the Fe-CMAS melt (compared to the Fe-MAS melt; Table 1) allows for an increased physical solubility of CO. Continuation of the reduction reaction, however, requires that CO molecules diffuse not through the original Fe-CMAS composition, but rather through the reduced, CO₃²⁻-bearing melt. A calculation of the molar volume for the reduced, carbonate-bearing Fe-CMAS, following the protocol of Lange and Carmichael (1987) and employing a partial molar volume for CO₂ (i.e., CO₃²⁻) of 24 cm³/mol (Spera and Bergman 1980; Lange 1994) and assuming that the limit of chemical dissolution of CO matches the conversion of all Fe³⁺ to Fe²⁺ following reaction Equation 9, indicates that the molar volume is little changed by the reaction. (Such a calculation also suggests that the chemically dissolved CO₃²⁻ in the reduced Fe-CMAS amounts to ~1.5 wt%.)

Thus, at the beginning of the experiment, the primary effect of the presence of CaO in the melt is to increase the chemical solubility of CO₃²⁻ and, in comparison to the Fe-MAS melt, to increase the molar volume and thus the physical solubility of CO. The effect of the incorporation of CO₃²⁻ (the chemical dissolution) is to consume electron holes while not decreasing the physical solubility of CO: Mode III reduction is shut down; the system cascades along the Mode I kinetic path.

The dynamics of Mode I reduction were explored for the incorporation of H₂ into a natural rhyolitic melt by Gaillard et al. (2003). They employed effectively an analysis, following Crank (1975), in which a significant gradient in molecular hydrogen concentration was anticipated in the distance we here describe

as Δξ. The analysis required the fitting of their kinetic data to discern and discriminate the H₂ concentration from the average self-diffusion coefficient. We do not have the same amount of data to follow effectively their approach to calculate D_{CO} in our experiments. Nevertheless, one realizes that the difference in concentration of physically dissolved CO between ξ' and ξ'' will actually be very small, i.e., at point-defect levels, i.e., ~10⁻⁷ atomic fraction, as evidenced by the constant composition indicated by the optical transmittance, that is, c_{CO} in the reacted melt is approximately constant. Consequently, employing an estimate of c_{CO}, one can follow the approach outlined in Equations 2 and 3 to calculate D_{CO}. In this case, the variable i ≡ CO, the value of λ remains the same (because 1 mole of CO reduces to reduce 1 mole of Fe₂O₃ in the melt) and there is no gradient in electrical potential. Realizing that between ξ' and ξ'', dμ_{CO} = -1/2dμ_{O₂}, one determines that the CO flux is given by

$$j_{\text{CO}} = \frac{c_{\text{CO}} D_{\text{CO}}}{2\Delta\xi} \int_{f_{\text{O}_2} @ \xi'}^{f_{\text{O}_2} @ \xi''} d \ln f_{\text{O}_2}. \quad (11)$$

Continuing, one notes: (1) c_{CO} ≡ X_{CO}/V_m and (2) evaluation of the integral above, with the limits of 1W-3 at ξ' and activity-modified FHQ at ξ'', gives 16.1; substituting into Equation 2:

$$\frac{d(\Delta\xi)}{dt} = j_{\text{CO}} V_m \lambda = \frac{16.1 \lambda X_{\text{CO}} D_{\text{CO}}}{2\Delta\xi}. \quad (12)$$

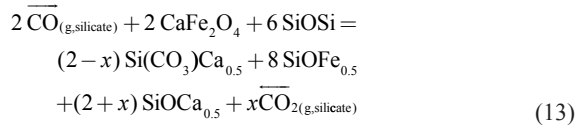
Separating variables and integrating gives the parabolic law (Eq. 1b) where, substituting for the value for λ, 2k' = 728.1X_{CO}D_{CO}.

The physical solubility of CO in a reduced basalt has not been measured. Similar in molecular size to Ar [as well as to H₂O (cf. Doremus 2002)], one anticipates, based on the model of ionic porosity, a similar physical solubility of CO and of Ar (Carroll and Stolper 1991; Shelby 1996). Carroll and Stolper (1993) report an argon solubility in a tholeiitic melt at 1400 °C as 6.6 × 10⁻⁹ mol/cm³, a value all-but-identical to that indicated by a conservative extrapolation of the data of Jambon and Shelby (1980). Employing the density model of Lange and Carmichael (1987) for the reduced melt in the region Δξ gives V_{m,1400 °C} ≈ 24 cm³/mol; thus, X_{CO} ≈ 1.6 × 10⁻⁷. For 2k' = 4.7 × 10⁻⁸ cm²/s (Fig. 6), substituting values into Equation 12 gives an average self-diffusion coefficient for CO of D_{CO,1400 °C} = 4.1 × 10⁻⁴ cm²/s. There is no other measurement of D_{CO} in the literature with which to compare this result (cf. Doremus 2002). The value, though, is somewhat slower than that of molecular H₂ in an obsidian melt [D_{H₂,1400 °C} = 7.9 × 10⁻⁴ cm²/s (Galliard et al. 2003)] and faster than molecular H₂O in a basaltic melt [assuming a molecular H₂O content of 1 wt%: D_{H₂O, 1400 °C}, 1 wt% = 2.1 × 10⁻⁵ cm²/s (Okumura and Nakashima 2006; Zhang et al. 2007)]; so bracketing this value for D_{CO,1400 °C} with that of molecular species of similar size indicates the reasonableness of our result (and of the

³CO + 1/2O₂ = CO₂; therefore, dμ_{CO} + 1/2dμ_{O₂} = dμ_{CO₂}. Across the reaction zone Δξ, however, the chemical potential of CO₂ is a constant, fixed by the chemical solubility of carbonate ions in the reacted/reduced melt. Thus, dμ_{CO₂} = 0 and dμ_{CO} = -1/2dμ_{O₂} (cf. Schmalzried 1983).

assumption concerning c_{CO}).

It bears mentioning that our value for $D_{\text{CO},1400^\circ\text{C}}$ is significantly higher (by two-plus orders of magnitude) than that described for molecular CO_2 or for “carbonate” (Watson et al. 1982; Fogel and Rutherford 1990; Nowak et al. 2004; Zhang et al. 2007). This result is significant in that, should the melt be unable to dissolve chemically as carbonate all of the CO_2 produced in the melt-reduction reaction, there would be a required, “outward” flux of the excess CO_2 , i.e., the reaction at ζ (cf. Eq. 9) would be modified to



where that portion of excess CO_2 is given by x ($0 \leq x \leq 2$) and the arrow indicates a flux toward the free surface. (This possibility is shown parenthetically in Fig. 1.) If one makes the reasonable assumption that the physical solubility of CO_2 in the reacted melt is similar to that of CO (though it is probably significantly less), a very small value of x , e.g., $\ll 10^{-2}$, would require the melt-reduction reaction rate be limited by the outward flux of CO_2 . Such kinetics would prove far too slow, given the community’s present understanding of D_{CO_2} and $D_{(\text{CO}_3)^{2-}}$: clearly, $x \approx 0$ in the reaction studied here.

Metal formation: FeO activity; SiO_2 reduction

The presence of metal at the surface of the samples indicates that the imposed f_{O_2} is low enough at the beginning of the experiment to reduce Fe^{2+} to Fe^0 . The fact that no metal is observed inside the reduced melt despite the presence of metal at the surface indicates that as the reactions that convert $\text{CO}_{(\text{g},\text{silicate})}$ to CO_3^- (Eqs. 8 and 9) proceed, the activity of FeO in the melt must be lowered to the point that metal formation is no longer thermodynamically favorable. Scrutiny of Equations 8 and 9, though, suggests that the carbonation reaction increases the activity of network-modifying Fe^{2+} . The contradiction suggests that the carbonated species in the reacted/reduced melt must include $2\text{Si}(\text{CO}_3)\text{Fe}_{0.5}$ [and $2\text{Si}(\text{CO}_3)\text{Mg}_{0.5}$] as well as the Ca^{2+} -bearing species; that is, a local equilibrium exists in which all three divalent network modifiers are bonded to CO_3^- , the ratio being set by the relative stability of the bonds [$|\Delta_r H|$] in the order $\text{Ca}^{2+} > \text{Mg}^{2+} \geq \text{Fe}^{2+}$ (Spera and Bergman 1980)], but that this equilibrium nevertheless lowers the activity of FeO enough such that iron metal cannot form, even at IW-4.5.

The metallic phase at the free surface of the droplets is iron in solution with silicon and carbon. The carbon content inferred for the metal, ≥ 4.4 at% for IW-4.5 specimens compared with a carbon activity of 0.12 in the $\text{CO}:\text{CO}_2$ environment, is consistent with the well-understood endothermic behavior of carbon in Fe-Si solutions (e.g., Darken and Gurry 1953). That the Si-bearing surface alloy was not seen for reduction of the Fe-MAS melt reacted under similar conditions of temperature and f_{O_2} indicates, at least, that the activity of SiO_2 in the original Fe-CMAS melt exceeded that for the Fe-MAS melt, which is evidenced in both the difference in silica content between the two starting compositions as well as in the difference in polymerization [NBO/T;

Table 1 (cf. Mysen and Richet 2005)]. Equally as significant, however, is the fact that the silicon inclusion in the alloy indicates an oxygen activity sufficiently low to have Si^{4+} be reduced to lower valence states. One anticipates $\text{Si}^{2+,3+}$ present in the melt and the redox buffering capacity of the melt so affected by the silica activity (e.g., Toropov and Barzakovskii 1966; Borman et al. 1991; Hosono et al. 1992). For the Fe-CMAS composition, this situation is not surprising since, of the major elements in the melt, Si is the second most noble metal species, one far more noble than Al, Mg, or Ca, that is $|\Delta_r G_{2\text{FeO}}^\circ| \ll |\Delta_r G_{\text{SiO}_2}^\circ| \ll |\Delta_r G_{2/3\text{Al}_2\text{O}_3}^\circ| < |\Delta_r G_{2\text{MgO}}^\circ| < |\Delta_r G_{2\text{CaO}}^\circ|$.⁴ Thus, another reaction, i.e., one similar to Equation 9 but which reduces network-forming Si^{4+} to, e.g., a network-modifier Si^{2+} and/or carbonate-bonded Si^{2+} is within reason—and within experience (e.g., Pettersen and Cooper 2008).

Calculations of the quantity of metallic iron-silicon-carbon alloy observed at the surface (for a sample reacted for 7040 s) show that the amount of iron precipitated at the surface corresponds to the amount of ionic iron contained in a ~ 15 μm layer of the original melt composition (calculations based on image analysis of Fig. 2). Assuming the precipitates are spherical with half of the sphere submerged in the melt, the maximum depth of the iron precipitates in the material is equivalent to the 15 μm thickness calculated for the depleted region. This correlation of precipitate depth and depletion depth suggests that the metal formation is essentially cut off once Mode II or III mechanisms are subjugated to Mode I.

Bubble formation: Closed-system redox upon quench

The presence of bubbles in the quenched specimens reacted at IW-4.5 implies that a reaction producing a gaseous phase is occurring either during the run of the experiment or upon quenching. Raman spectroscopy demonstrates that the bubbles formed in regions not affected by the Pt wire cage contain pure $\text{CO}_{(\text{g})}$, with some evidence of gas molecule adhesion to the silicate walls of the bubble (the carbonyl species; Fig. 7a); those bubbles in contact with the Pt wire, however, contained $\text{CO}_2(\text{g})$ and had their surfaces coated, at least in part, with condensed carbon, a clearly metastable assemblage (Fig. 7b). The former observation speaks to the internal redox dynamics associated with a closed-system quench and we here emphasize those physics. The latter observation speaks of oxidation catalysis associated with Pt. These data (i.e., Fig. 7b) are included because they are interesting, but will not be considered further.

It is impossible to form internal bubbles in an isothermal, open-system experiment in which a melt is exposed to a gas, even a noble gas like Ar or He where no sort of chemical dissolution reaction is possible. The increase in Gibbs energy associated with formation of the gas-melt interface is preclusive. The source of bubbles upon quench, however, is potentially possible for a physically dissolved gas species. The physical solubility is dic-

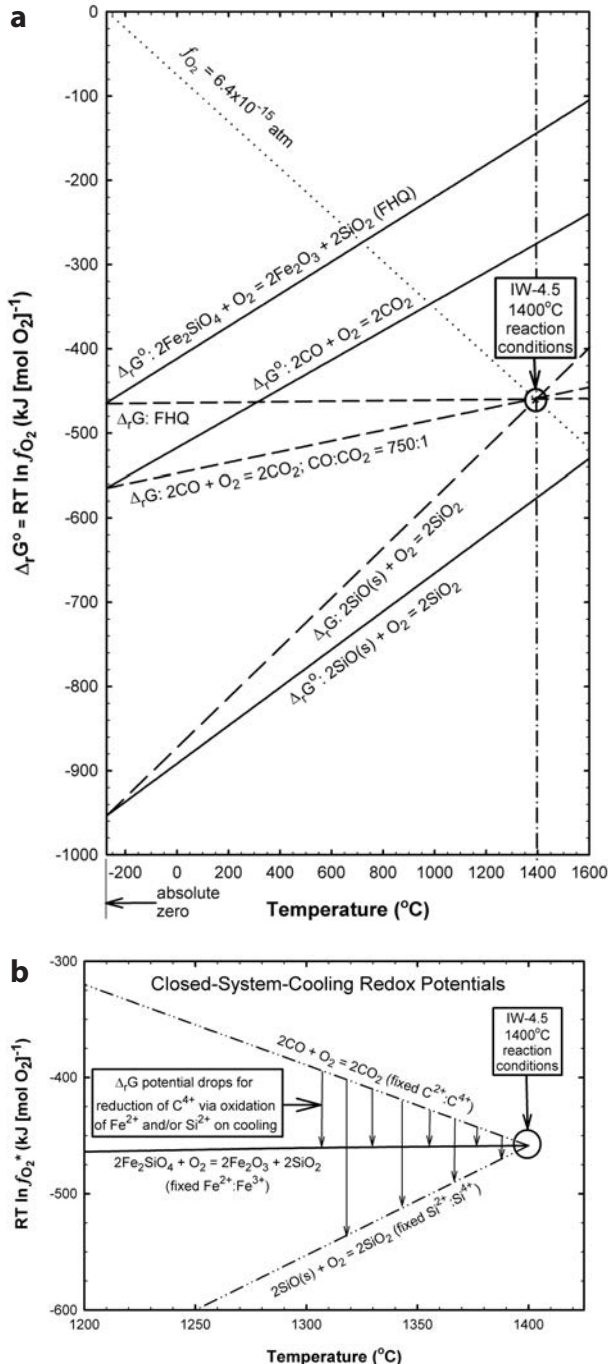
⁴These standard Gibbs energies of reaction ($\Delta_r G^\circ$) are for creation of pure oxides from pure metals (each with activity unity), written so as to consume 1 mole of pure $\text{O}_2(\text{g})$ —hence the coefficients in the identifying subscripts. These are the data presented on a standard Ellingham diagram (e.g., Fig. 8a); they inform an understanding of the relative oxidation potentials of pure metals.

tated by the “free volume” or ionic porosity of the melt [$\sim 45\%$ of the molar volume (e.g., Doremus 2002; cf. Carroll and Stolper 1991)]. The contraction associated with thermal quenching also reduces the volume associated with the ionic porosity creating a potential for exsolution, in part, of the physically dissolved CO . A calculation of the thermal contraction between 1400 and 600 $^{\circ}\text{C}$ (which is below the glass-transition temperature) for the re-acted/reduced Fe-CMAS melt, based on the model of Lange and Carmichael (1987) (which includes changes with temperature of both bond angle and bond length), suggests a total volume

reduction of only 3.4%; the effect on physical solubility of such a modest contraction is logically argued to be small.

The reduction reactions described in Equations 8 and 9, however, store carbon as C^{4+} in a medium that includes a notable quantity of Fe^{2+} ($\pm \text{Si}^{2+}$). During quenching, under the conditions where thermal flux far outstrips in rate any chemical diffusion flux, closed-system conditions can result in a reverse reaction occurring internally. A useful way of contemplating the thermodynamics of the forward, open-system reduction and the reverse, closed-system oxidation reactions is to employ an Ellingham (1944) diagram, in which (in general) the oxidation potential of various metals and metal oxides are plotted as a function of temperature. The standard form of the diagram is to plot $\Delta_r G_i^{\circ}$ vs. T ; by definition, $\Delta_r G_i^{\circ}$ is for the reaction where all products and reactants are at activity unity. If the reactions plotted each involve 1 mole of $\text{O}_{2(g)}$, the relative oxidation potentials of pure metals and pure oxides are revealed; further, because the reactions are described for 1 mole of O_2 , $\Delta_r G_i^{\circ} = RT \ln f_{\text{O}_2}$; thus, any line passing through the origin of the plot (zero Kelvin, zero Gibbs energy) is a locus of constant oxygen fugacity (slope = $R \ln f_{\text{O}_2}$).

Figure 8a presents an Ellingham diagram for the redox equilibria of particular interest in this study, i.e., $\text{Fe}^{2+,3+}$ and $\text{C}^{2+,4+}$, along with that of $\text{Si}^{2+,4+}$, which we argue as significant in this case. The solid curves in Figure 8a are the standard, $\Delta_r G_i^{\circ}$ reactions, and are essentially lines. The dominant temperature sensitivity of the oxidation reactions is the blatant one, i.e., $\Delta_r G_i^{\circ} = \Delta_r H_i^{\circ} - T\Delta_r S_i^{\circ}$, where H is enthalpy and S is entropy (that is, the temperature dependencies of H and S are distinctly second-order effects). The slopes of the Ellingham $\Delta_r G_i^{\circ}$ lines are ~ 200 J/(mol-K) and represent the entropy loss associated with the consumption of 1 mole of a diatomic gas (O_2). The $\text{Fe}^{2+,3+}$ reaction presented is for the FHQ equilibrium, presented earlier in



◀ **FIGURE 8.** Thermodynamic analysis associated with open-system reduction and closed-system (redox-couple) quenching. (a) Ellingham diagram of $\Delta_r G_i^{\circ}$ vs. temperature. The reference reactions (shown as solid lines) are for mineral (or gasses in the case of carbon oxides) and oxygen activities of unity. Consequently, (1) the value of $\Delta_r G_i^{\circ}$ is equal to the natural logarithm of the equilibrium oxygen fugacity multiplied by RT and (2) the slope of any line through the graph's origin (zero Kelvin, zero free energy) is one of constant f_{O_2} . All oxidation reactions are written in terms of 1 mole of O_2 ; as such, the relative oxidation potentials are revealed. Mixing $\text{CO}:\text{CO}_2$ at 750:1 (carbon oxide dashed line) and setting the temperature to 1400 $^{\circ}\text{C}$ (dash-dot line) sets the environment at $f_{\text{O}_2} = 6.4 \times 10^{-15}$ atm, which is IW-4.5 (the small circle). For the melt to come into equilibrium with this environment, the activities of the fayalite, hematite, silica, SiO , and carbon-oxide species in the melt must all be adjusted to be in equilibrium with the reaction conditions. The Ellingham $\Delta_r G_i^{\circ}$ lines rotate around their respective zero-Kelvin (-273 $^{\circ}\text{C}$) intercepts forming the $\Delta_r G_i^{\circ}$ lines (dashed). (b) Upon quench, one can calculate an effective $f_{\text{O}_2}^*$ based upon a fixed amount of various-valence cations (e.g., $\text{Fe}^{2+,3+}$ for the FHQ reaction): the critical physical entity is the relative temperature sensitivities of the component activity coefficients. In this figure, the $f_{\text{O}_2}^*$ was calculated directly for the reduced Fe-CMAS melt using the thermodynamic model MELTS (thus it is plotted as a solid line). The arguments for the relative placement of the $\text{C}^{2+,4+}$ and $\text{Si}^{2+,4+}$ lines are made in the text. Cooling in closed-system quench creates a $\Delta_r G_i^{\circ}$ driving potential (the fine, downward-pointing arrows) for the reduction of C^{4+} (carbonate) via the (re)oxidation of Fe^{2+} and Si^{2+} : this is the potential drop realized in the formation of the CO gas bubbles during quench.

reference to MELTS (Ghiorso and Sack 1995). When reactants or products of the reactions are dissolved in solution, one must describe $\Delta_r G_i$, instead of $\Delta_r G_i^\circ$, the relationship being, e.g., for the case of the schematic reaction $4\text{AO} + \text{O}_{2(\text{g})} = 2\text{A}_2\text{O}_3$:

$$\Delta_r G_{\text{AO-A}_2\text{O}_3} = \Delta_r G_{\text{AO-A}_2\text{O}_3}^\circ + RT \ln \left(\frac{a_{\text{A}_2\text{O}_3}^2}{a_{\text{AO}}^4 f_{\text{O}_2}} \right) \quad (14)$$

where a_i is activity of species i . To plot this $\Delta_r G_i$ on the Ellingham diagram, the f_{O_2} is still calculated as unity (e.g., Paul 1990a). One sees that the far right-hand term is linear in T ; $\Delta_r G_i^\circ$ is also recognized to be linear in T : thus, the adjustment of activities because of the involvement of reactants or products in solution simply cause rotation of the $\Delta_r G_i^\circ$ Ellingham line around its zero-Kelvin intercept. In Figure 8a, the open system reaction condition for the 1400 °C, IW-4.5 experiments is identified and plotted by rotating the $\Delta_r G_{\text{CO-CO}_2}^\circ$ line for the conditions $(a_{\text{CO}_2}^2/a_{\text{CO}}^2) = (1/750)^2$ and noting the point (circled) where this $\Delta_r G_{\text{CO-CO}_2}$ line (dashed) intersects 1400 °C—which is at $-458.6 \text{ kJ} [\text{mol O}_2]^{-1}$; the slope of the line passing from this point through the plot origin (dotted) is $R \ln f_{\text{O}_2}$ for $f_{\text{O}_2} = 6.4 \times 10^{-15}$ atm. For the melt to come into equilibrium with this 1400 °C, IW-4.5 condition, the activities and, thus, the concentrations, of Fe_2SiO_4 , Fe_2O_3 , SiO , and SiO_2 must evolve so as to rotate the respective Ellingham lines to the $\Delta_r G_i$ positions (dashed in Fig. 8a).

Quenching involves the removal of heat, in which the dissipation of thermal energy happens at a rate that prevents chemical diffusion. The thermal diffusivity in silicate glassmelts at temperatures ~ 1400 °C is on the order of $10^{-2} \text{ cm}^2/\text{s}$ (Allen et al. 1994); chemical diffusivities are at least two orders of magnitude smaller (as evidenced here, for example). Thus the system becomes closed (e.g., Darken and Gurry 1953), that is, there is no longer any communication with the environment via chemical diffusion and only local redox adjustments can occur. The driving potentials for these local redox couples can be illustrated using an extension of the Ellingham diagram (e.g., Paul 1990b). In quenching, the ratio of the heterovalent states of an ion are fixed (i.e., one cannot add or subtract chemical species—ions or electrons—to effect a change in the ratio). Thus, while, e.g., the mole fractions of the fayalite, hematite, and silica components in the melt, X_{Fa} , X_{Hem} , and X_{Qtz} , respectively, are fixed, the activity coefficients, γ_{Fa} , γ_{Hem} , and γ_{Qtz} will change with decreasing temperature. One can calculate, therefore, an “effective” oxygen fugacity [$f_{\text{O}_2}^*(T)$] for quenching. In the case of the FHQ reaction, $2\text{Fe}_2\text{SiO}_4 + \text{O}_{2(\text{g})} = 2\text{Fe}_2\text{O}_3 + 2\text{SiO}_2$, one is solving the mass-action equation

$$\begin{aligned} \Delta_r G_{1673\text{K}} &= -458.6 \text{ kJ} [\text{mol O}_2]^{-1} \\ &= \Delta_r G_{r,\text{FHQ}}^\circ + RT \ln \left[\frac{(\gamma_{\text{Hem}}^2 X_{\text{Hem}}^2)(\gamma_{\text{Qtz}}^2 X_{\text{Qtz}}^2)}{(\gamma_{\text{Fa}}^2 X_{\text{Fa}}^2)(f_{\text{O}_2}^*)} \right] \end{aligned} \quad (15)$$

for $f_{\text{O}_2}^*$ as a function of T , holding the mole fractions of the condensed components fixed. The calculation reveals the solid-line $\Delta_r G_{\text{FHQ}}$ potential “path,” starting at the 1400 °C, IW-4.5 conditions, shown in Figure 8b. (This path has a slightly steeper slope than the $\Delta_r G_{\text{FHQ}}$ line shown in Figure 8a; this path is straight-

forwardly calculated using MELTS.)

Unfortunately, despite the careful characterization of the pressure sensitivity of γ_{CO_2} [see the many references cited near Eqs. 7 and 8, as well as Dixon (1997)], the temperature sensitivities of the activity coefficients for the carbon oxide and silicon monoxide species have not been well characterized. Still, one can make some inferences based on the behaviors seen in a wide variety of studies. In the case of the reaction $2\text{CO} + \text{O}_2 = 2\text{CO}_2$, the behavior of $\gamma_{\text{CO}_2}^2/\gamma_{\text{CO}}^2$ as temperature falls is in question (cf. Eq. 15). Both γ_{CO_2} and γ_{CO} are >1 (the solutions are endothermic). With a decrease in temperature, both activity coefficients should increase. The increase of γ_{CO_2} should far outstrip that of γ_{CO} . CO in physical solution is only affected by the thermal expansion while CO_2 (as CO_3^{2-}) is in a highly endothermic chemical solution (e.g., Spera and Bergman 1980). As such, the $\Delta_r G_{\text{CO-CO}_2}$ path on quenching should have a steep, negative slope, as represented by the dash-dot-dot line in Figure 8b. The argument for the reaction $2\text{SiO} + \text{O}_2 = 2\text{SiO}_2$ is similar, although the result contrasts significantly: γ_{SiO_2} is <1 (exothermic) for silicate melts of polymerization similar to that of the FeCMAS composition, but would decrease but slightly with decreasing temperature (e.g., Hess 1995). Based on its apparent limited solubility, γ_{SiO} is anticipated as >1 (e.g., Toropov and Barzakovskii 1966) and should increase significantly with temperature. Thus, the $\Delta_r G_{\text{SiO-SiO}_2}$ path on quenching should have a distinct positive slope (labeled dash-dot-dot line in Fig. 8b). One can therefore identify the increasing driving potential for reduction of C^{4+} by the acceptance of electrons from Fe^{2+} and Si^{2+} as the vertical distance on the plot, increasing with magnitude as temperature is lowered, represented by the fine, downward-pointing arrows in Figure 8b. Quenching rate, which is not characterized on a thermodynamic plot like the Ellingham diagram, affects the reaction extent during cooling. Electron transfer kinetics are a function of the spatial distribution of carriers (e.g., Zarzycki 1991). One can imagine quenching a specimen rapidly enough so as to have little of the closed-system reaction taking place. In the IW-4.5 specimens, this is clearly not the case, as evidenced by the formation of the CO-filled bubbles.

This analysis is consistent fully with the argument of Mathez (1984) concerning the role of isobaric degassing, particularly of carbon oxides, in affecting the redox state of basaltic magmas and lavas. The reaction shown here as Equation 9, run in reverse, is the equivalent of Mathez’s Equation 3a. The Ellingham-Diagram analysis demonstrates the sources and sinks, both “local,” for the electrons in the reaction, as well as emphasizing the role of temperature in effecting chemical solubility.

This exact type of redox adjustment upon quenching accounts, too, for the formation of Pt metal colloids (“micronuggets”) in multicomponent silicate melts that are in contact with bulk Pt (e.g., Ginther 1971; Cottrell and Walker 2006; cf. Palme 2008). With initial contact of a PtO [or PtO₂ (Farges et al. 1999)]-free silicate with Pt at elevated temperature, there exists an extreme chemical potential gradient for the oxidation of the Pt coupled with the reduction of various cation species in the melt; the overall reaction is one both of reduction of the silicate and formation of a solution that contains ionic platinum [the thermodynamics of similar metal-silicate reactions is presented in Cook and Cooper (1999)]. The oxidation of Pt is an endothermic

reaction as is its incorporation into the silicate melt, both serve to make the $\Delta_r G_{\text{Pt-PtO}}$ vs. T closed-system path have a sharply negative slope, allowing Si^{2+} and Fe^{2+} to reduce ionic Pt to metal upon quenching. The results of the Cottrell and Walker (2006) experiments on the reaction of mafic liquids with both Pt and graphite (the experimental capsule material) at 2500 °C, 2.2 GPa conditions are particularly remarkable in that portions of their experimental charges cooled rapidly enough upon quench to keep ionic Pt and carbonate in solution while in portions of the specimen cooling more slowly (near its center) developed both Pt metal micronuggets and (surprisingly, given the high pressure) vesicles filled with CO.

Reduction of a tholeiitic basaltic melt

As mentioned earlier, these same reduction experiments were initially conducted on a tholeiitic basalt from the Columbia River Plateau [the bulk composition given in Cooper et al. (1996)]. Kinetically and morphologically, the results were essentially identical to those seen for the Fe-CMAS melts. The reaction occurred much more slowly than for the Fe-MAS melt and liquids (suspended droplet specimens) reacted (1) at IW-3, 1380 °C formed fine iron-alloy, molten (at temperature) precipitates on their free surface, of the same scale as seen in Figure 2, while those reacted (2) at IW-4.5, 1380 °C saw formation of bubbles upon quenching. No internal metal colloid/precipitates were found. A significant difference between the basalt and the Fe-CMAS specimens was the composition of the surface alloy formed. In the case of the basalt, the alloy included (from EDS analyses) ~8 at% phosphorous, ~2 at% sulfur, and ~1 at% silicon. Unlike the case for Fe-CMAS, estimating the amount of carbon in the alloy based on the morphology is not straightforward. This amount of P alone is enough to exceed the liquidus temperature of an Fe-P alloy at $T \sim 1200$ °C and form a partial melt at $T \sim 1050$ °C (Raghavan 2004). That the alloy should get P and S from the melt is not surprising since $|\Delta_r G_{\text{SiO}_2}^\circ| < |\Delta_r G_{\text{FeO}}^\circ| < |\Delta_r G_{\text{SiO}_2/\text{SiO}_5}^\circ| < |\Delta_r G_{\text{SiO}_2}^\circ|$. Nevertheless, the overall dynamic in the basalt reflects the behavior of Fe-CMAS, that is, reduction in a CO-rich environment is accomplished by molecular diffusion of CO and the reaction manifest is the formation of carbonate species within the melt, which lowers the activity of FeO enough, even at IW-4.5, so as to prohibit the internal precipitation of metal.

CONCLUDING REMARKS

Reduction of Fe-CMAS melt in a $\text{CO}:\text{CO}_2$ gaseous buffer, in the absence of convection in the liquid, is a diffusion-limited reaction that is rate limited by flux of molecular CO through the reduced melt. The reduced melt is one that incorporates carbon as C^{4+} (carbonate), the C^{2+} being oxidized via reduction of the more-noble components in the original silicate melt, specifically $\text{Fe}^{3+} \pm \text{Si}^{4+}$. A significant amount of C^{4+} can be so incorporated at the low f_{O_2} studied here. Carbonate formation lowers the activity of FeO sufficiently such that metallic iron (or an iron alloy) does not form internally, even at (T, f_{O_2}) conditions more extreme than those that did result in internal formation of metal in a similarly polymerized, but CaO-free melt. Quenching reveals closed-system behavior, based on the relative temperature sensitivities of the activity coefficients for various heterovalent-cation species, that emphasizes/accesses local redox couples.

Broad application of the results from this study requires reflection. The experiments indicate that the Mode III reduction dynamic (based on coupled cation and electron hole fluxes) most likely will not dominate the evolution of texture, e.g., in chondrules. Furthermore, a carbon-oxide gas is not representative of the nebular environment. Experiments in a H_2 -rich gas are required. One anticipates that reduction experiments in $\text{H}_2:\text{H}_2\text{O}$ to a similar (T, f_{O_2}) condition (IW-4.5 at 1400 °C would require an $\text{H}_2:\text{H}_2\text{O}$ ratio of ~300:1) would see kinetics rate-limited by diffusion of molecular H_2 (cf. Gaillard et al. 2003). The possibility of forming metal internally will depend on the incorporation of oxidized hydrogen and its effect on the activity of FeO. The experiments reported here, and particularly in their comparison, e.g., to melt reaction experiments involving carbon containment capsules (e.g., Fogel and Rutherford 1995; Cottrell and Walker 2006), additionally raise questions about the speciation and transport of carbon species in silicate melts. Both the hydrogen and carbon effects on redox dynamics remain fruitful directions for further research.

ACKNOWLEDGMENTS

The authors acknowledge helpful, wide-ranging discussions with Mac Rutherford and Paul Hess about aspects of this work. The manuscript was improved significantly based upon several insightful, formal reviews, but particularly those by Fabrice Gaillard, Frank Spera, and Don Baker. The research reported here was financially supported, in part, by grants (to R.F.C.) from the National Science Foundation (CTS-0405063 and EAR-0538170).

REFERENCES CITED

- Allen, W.P., Bromwell, D., Doyle, T., Devlin, L., Snider, R., Watson, P., and Dixon, G. (1994) Thermal transport in silicate glasses. II. Extended phonons. *Physical Review B*, 49, 265–270.
- Borman, V.D., Gusev, E.P., Lebedinskii, Y.Y., and Troyan, V.I. (1991) Direct observation of the layer-by-layer growth of initial oxide layers on Si(100) surface during thermal oxidation. *Physical Review Letters*, 67, 2387–2390.
- Brooker, R.A., Kohn, S.C., Holloway, J.R., and McMillan, P.F. (2001a) Structural controls on the solubility of CO_2 in silicate melts Part I: Bulk solubility data. *Chemical Geology*, 174, 225–239.
- (2001b) Structural controls on the solubility of CO_2 in silicate melts Part II: IR characteristics of carbonate groups in silicate glasses. *Chemical Geology*, 174, 241–254.
- Carroll, M.R. and Stolper, E.M. (1991) Argon solubility and diffusion in silica glass: Implications for the solution behavior of molecular gasses. *Geochimica et Cosmochimica Acta*, 55, 211–225.
- (1993) Noble gas solubilities in silicate melts and glasses: New experimental results for argon and the relationship between solubility and ionic porosity. *Geochimica et Cosmochimica Acta*, 57, 5039–5051.
- Cook, G.B. and Cooper, R.F. (1999) Redox dynamics in the high-temperature float processing of glasses. I. Reaction between undoped and iron-doped borosilicate glassmelts and a gold-tin alloy. *Journal of Non-Crystalline Solids*, 249, 210–227.
- (2000) Iron concentration and the physical processes of dynamic oxidation in an alkaline earth aluminosilicate glass. *American Mineralogist*, 85, 397–406.
- Cook, G.B., Cooper, R.F., and Wu, T. (1990) Chemical diffusion and crystalline nucleation during oxidation of ferrous iron-bearing magnesium aluminosilicate glass. *Journal of Non-Crystalline Solids*, 120, 207–222.
- Cooper, R.F., Fanselow, J.B., Weber, J.K.R., Merkle, D.R., and Paker, D.B. (1996) Dynamics of oxidation of a Fe^{2+} -bearing aluminosilicate (basaltic) melt. *Science*, 274, 1173–1176.
- Cottrell, E. and Walker, D. (2006) Constraints on core formation from Pt partitioning in mafic silicate liquids at high temperatures. *Geochimica et Cosmochimica Acta*, 70, 1565–1580.
- Crank, J. (1975) *The Mathematics of Diffusion*, 414 p. Clarendon Press, Oxford.
- Darken, L.S. and Gurry, R.W. (1953) *Physical Chemistry of Metals*, 535 p. McGraw-Hill, New York.
- Dixon, J.E. (1997) Degassing of alkaalic basalts. *American Mineralogist*, 82, 368–378.
- Dixon, J.E., Stolper, E.M., and Holloway, J.R. (1995) An experimental study of water and carbon dioxide solubilities in mid-ocean ridge basaltic liquids. Part I: Calibration and solubility models. *Journal of Petrology*, 36, 1607–1631.

- Doremus, R.H. (2002) Diffusion of Reactive Molecules in Solids and Melts, 293 p. Wiley, New York.
- Dunn, T. (1982) Oxygen diffusion in three silicate melts along the join diopside-anorthite. *Geochimica et Cosmochimica Acta*, 46, 2293–2299.
- Eggler, D.H., Mysen, B.O., Hoering, T.C., and Holloway, J.R. (1979) The solubility of carbon monoxide in silicate melts at high pressures and its effect on silicate phase relations. *Earth and Planetary Science Letters*, 43, 321–330.
- Ellingham, H.J.T. (1944) Reducibility of oxides and sulfides in metallurgical processes. *Journal of the Society of Chemical Industry*, 63, 125–133.
- Everman, R.L.A. and Cooper, R.F. (2003) Internal reduction of an iron-doped magnesium aluminosilicate melt. *Journal of the American Ceramic Society*, 86, 487–494.
- Farges, F., Neuville, D.R., and Brown Jr., G.E. (1999) Structural investigation of platinum solubility in silicate glasses. *American Mineralogist*, 84, 1562–1568.
- Ferrari, A.C. and Robertson, J. (2002) Interpretation of Raman spectra of disordered and amorphous carbon. *Physical Review B*, 61, 14095–14107.
- Fine, G. and Stolper, E. (1985/86) Dissolved carbon dioxide in basaltic glasses: Concentrations and speciation. *Earth and Planetary Science Letters*, 76, 263–278.
- Fogel, R.A. and Rutherford, M.J. (1990) The solubility of carbon dioxide in rhyolitic melts: A quantitative FTIR study. *American Mineralogist*, 75, 1311–1326.
- (1995) Magmatic volatiles in primitive lunar glasses. I. FTIR and EMPA analyses of Apollo 15 green and yellow glasses and revision of the volatile-assisted fire-fountain theory. *Geochimica et Cosmochimica Acta*, 59, 201–215.
- Gaillard, F., Schmidt, B., Mackwell, S., and McCammon, C. (2003) Rate of hydrogen-iron redox exchange in silicate melts and glasses. *Geochimica et Cosmochimica Acta*, 67, 2427–2441.
- Ghiorso, M.S. and Sack, R.O. (1995) Chemical mass transfer in magmatic processes IV: A revised and internally consistent thermodynamic model for the interpolation and extrapolation of liquid-solid equilibria in magmatic systems at elevated temperatures and pressures. *Contributions to Mineralogy and Petrology*, 119, 197–212.
- Ginther, R.J. (1971) The contamination of glass by platinum. *Journal of Non-Crystalline Solids*, 6, 294–306.
- Greaves, G.N. (1985) EXAFS and the structure of glass. *Journal of Non-Crystalline Solids*, 71, 203–217.
- Grove, T.L. (1981) Use of FePt alloys to eliminate the iron loss problem in 1 atmosphere gas mixing experiments; theoretical and practical considerations. *Contributions to Mineralogy and Petrology*, 78, 298–304.
- Hess, P.C. (1980) Polymerization model for silicate melts. In R.B. Hargraves, Ed., *Physics of Magmatic Processes*, p. 3–48. Princeton University Press, New Jersey.
- (1995) Thermodynamic mixing properties and the structure of silicate melts. In J.F. Stebbins, P.F. McMillan, and D.B. Dingwell, Eds., *Structure, Dynamics, and Properties of Silicate Melts*, 32, p. 145–189. Reviews in Mineralogy, Mineralogical Society of America, Chantilly, Virginia.
- Hosono, H., Abe, Y., Kinser, D.L., Weeks, R.A., Muta, K., and Kawazoe, H. (1992) Nature and origin of the 5-eV band in SiO₂:GeO₂ glasses. *Physical Review B*, 46, 11445–11451.
- Jambon, A. and Shelby, J.E. (1980) Helium diffusion and solubility in obsidians and basaltic glass in the range 200–300°C. *Earth and Planetary Science Letters*, 51, 206–214.
- Jurado-Egea, J.R., Owen, A.E., and Bandyopadhyay, A.K. (1987) Electronic conduction in basalt glass and glass-ceramics: Correlation with magnetite crystallization. *Journal of Materials Science*, 22, 3602–3606.
- Kessel, R., Beckett, J.R., and Stolper, E.M. (2001) Thermodynamic properties of the Pt-Fe system. *American Mineralogist*, 86, 1003–1014.
- King, E.A. (1983) Reduction, partial evaporation, and spattering: possible chemical and physical processes in fluid drop chondrule formation. In E.A. King, Ed., *Chondrules and their Origins*, p. 180–187. Lunar and Planetary Institute, Houston, Texas.
- Kondepudi, D. and Prigogine, I. (1998) *Modern Thermodynamics: From heat engines to dissipative structures*, 486 p. Wiley, New York.
- Kong, P. and Palme, H. (1999) Compositional and genetic relationship between chondrules, chondrule rims, metal, and matrix in the Renazzo chondrite. *Geochimica et Cosmochimica Acta*, 63, 3673–3682.
- Kubaschewski, O., Evans, E.L., and Alcock, C.B. (1967) *Metallurgical Thermochemistry*, 495 p. Pergamon Press, Oxford, U.K.
- Lange, R.A. (1994) The effect of H₂O, CO₂, and F on the density and viscosity of silicate melts. In M.R. Carroll and J.R. Holloway, Eds., *Volatiles in Magmas*, 30, p. 331–369. Reviews in Mineralogy, Mineralogical Society of America, Chantilly, Virginia.
- Lange, R.A. and Carmichael, I.S.E. (1987) Densities of Na₂O-K₂O-CaO-MgO-FeO-Fe₂O₃-Al₂O₃-TiO₂-SiO₂ liquids: New measurements and derived partial molar properties. *Geochimica et Cosmochimica Acta*, 51, 2931–2946.
- Lee, M.S., Rubin, A.E., and Wasson, J.T. (1992) Origin of metallic Fe-Ni in Renazzo and related chondrites. *Geochimica et Cosmochimica Acta*, 56, 2521–2533.
- Libourel, G., Krot, A.N., and Tissandier, L. (2006) Role of gas-melt interaction during chondrule formation. *Earth and Planetary Science Letters*, 251, 232–240.
- Mathez, E.A. (1984) Influence of degassing on oxidation states of basaltic magmas. *Nature*, 310, 371–375.
- Mendybaev, R.A., Beckett, J.R., Stolper, E.M., and Grossman, L. (1998) Measurement of oxygen fugacities under reducing conditions: Non-nernstian behavior of Y₂O₃-doped zirconia oxygen sensors. *Geochimica et Cosmochimica Acta*, 62, 3131–3139.
- Mendybaev, R.A., Beckett, J.R., Grossman, L., Stolper, E., Cooper, R.F., and Bradley, J.P. (2002) Volatilization kinetics of silicon carbide in reducing gases: An experimental study with applications to the survival of presolar grains in the solar nebula. *Geochimica et Cosmochimica Acta*, 66, 661–682.
- Myers, J. and Eugster, H.P. (1983) The system Fe-Si-O; oxygen buffer calibrations to 1500 K. *Contributions to Mineralogy and Petrology*, 82, 75–90.
- Mysen, B.O. (1988) *Structure and Properties of Silicate Melts*, 354 p. Elsevier, Amsterdam.
- Mysen, B.O. and Richet, P. (2005) *Silicate Glasses and Melts: Properties and Structure*, 544 p. Elsevier, Amsterdam.
- Mysen, B.O., Virgo, D., Neumann, E., and Seifert, F.A. (1985) Redox equilibria and the structural states of ferric and ferrous iron in melts in the system CaO-MgO-Al₂O₃-SiO₂-FeO: Relationships between redox equilibria, melt structure and liquidus phase equilibria. *American Mineralogist*, 70, 317–331.
- Nowak, M., Porbatzki, D., Spickenbom, K., and Diedrich, O. (2003) Carbon dioxide speciation in silicate melts: A restart. *Earth and Planetary Science Letters*, 207, 131–139.
- Nowak, M., Schreen, D., and Spickenbom, K. (2004) Argon and CO₂ on the race track in silicate melts: A tool for the development of a CO₂ speciation and diffusion model. *Geochimica et Cosmochimica Acta*, 68, 5127–5138.
- Nowok, J.W. (1995) Viscosity and structural state of iron in coal ash slags under gasification conditions. *Energy and Fuels*, 9, 534–539.
- Okumura, S. and Nakashima, S. (2006) Water diffusion in basaltic to dacitic glasses. *Chemical Geology*, 227, 70–82.
- Palme, H. (2008) Platinum-group elements in cosmochemistry. *Elements*, 4, 233–238.
- Pantano, C.G., Singh, A.K., and Zhang, H. (1999) Silicon oxycarbide glasses. *Journal of Sol-Gel Science and Technology*, 14, 7–25.
- Paul, A. (1990a) *Chemistry of Glasses*, 380 p. Chapman and Hall, London.
- (1990b) Oxidation-reduction equilibrium in glass. *Journal of Non-Crystalline Solids*, 123, 354–362.
- Pawley, A.R., Holloway, J.R., and McMillan, P.F. (1992) The effect of oxygen fugacity on the solubility of carbon-oxygen fluids in basaltic melt. *Earth and Planetary Science Letters*, 110, 213–225.
- Pettersen, C. and Cooper, R.F. (2008) Float-reaction between liquid bronze and magnesium aluminosilicate and ZnO-doped magnesium aluminosilicate glass-ceramic-forming glassmelts. *Journal of Non-Crystalline Solids*, 354, 3194–3206.
- Pommier, A., Gaillard, F., and Pichavant, M. (2008) Modeling the time-dependent changes in electrical conductivity of basaltic melts with redox state. EOS: Transactions of the American Geophysical Union, 89, Fall Meeting Supplement, Abstract MR21C-07.
- Raghavan, V. (1986) The carbon-iron-silicon system. *Journal of Alloy Phase Diagrams*, India, 2, 97–107.
- (2004) C-Fe-P (carbon-iron-phosphorous). *Journal of Phase Equilibria and Diffusion*, 25, 541–542.
- Schmalzried, H. (1981) *Solid State Reactions*, 254 p. Verlag Chemie, Weinheim, Germany.
- (1983) Internal and external oxidation of nonmetallic compounds and solid solutions (I). *Berichte der Bunsen-Gesellschaft für Physikalische Chemie*, 87, 551–558.
- (1984) Oxide solid solutions and its internal reduction reactions. *Berichte der Bunsen-Gesellschaft für Physikalische Chemie*, 88, 1186–1191.
- Schofield, P.F., Cressey, G., Wren Howard, P., and Henderson, C.M.B. (1995) Origin of colour in iron and manganese containing glasses investigated by synchrotron radiation. *Glass Technology*, 36, 89–94.
- Shelby, J.E. (1996) *Handbook of Gas Diffusion in Solids and Melts*, 240 p. ASM International, Materials Park, Ohio.
- Smith, D.R. and Cooper, R.F. (2000) Dynamic oxidation of a Fe²⁺-bearing calcium-magnesium-aluminosilicate glass: The effect of molecular structure on chemical diffusion and reaction morphology. *Journal of Non-Crystalline Solids*, 278, 145–163.
- Speight, J.G. (2005) *Lange's Handbook of Chemistry*, 1000 p. McGraw-Hill, New York.
- Spera, F.J. and Bergman, S.C. (1980) Carbon dioxide in igneous petrogenesis: I—Aspects of the dissolution of CO₂ in silicate liquids. *Contributions to Mineralogy and Petrology*, 74, 55–66.
- Thibault, Y. and Holloway, J.R. (1994) Solubility of CO₂ in a Ca-rich leucite: Effects of pressure, temperature and oxygen fugacity. *Contributions to Mineralogy and Petrology*, 116, 216–224.

- Toropov, N.A. and Barzakovskii, V.P. (1966) High-Temperature Chemistry of Silicates and Other Oxide Systems, 216 p. Consultants Bureau/Plenum, New York.
- Wagner, C. (1959) Reaktionstypen bei der oxydation von legierungen. Zeitschrift für Elektrochemie, 63, 772–782.
- Wasson, J.T. (1985) Meteorites: Their Record of Early Solar System History, 267 p. W.H. Freeman, New York.
- Watson, E.B., Sneeringer, M.A., and Ross, A. (1982) Diffusion of dissolved carbonate in magmas: Experimental results and applications. Earth and Planetary Science Letters, 61, 346–358.
- Weyl, W.A. (1951) Coloured Glasses, 541 p. Society of Glass Technology, Sheffield, U.K.
- Wopenka, B. and Pasteris, J.D. (1987) Raman intensities and detection limits of geochemically relevant gas mixtures for a laser Raman microprobe. Analytical Chemistry, 59, 2165–2170.
- Zallen, R. (1983) The Physics of Amorphous Solids, 304 p. Wiley, New York.
- Zarzycki, J. (1991) Glasses and the Vitreous State, 505 p. Cambridge University Press, Cambridge, U.K.
- Zhang, Y., Xu, Z., Zhu, M., and Wang, H. (2007) Silicate melt properties and volcanic eruptions. Reviews of Geophysics, 45, RG4004, DOI: 10.1029/2006RG000216.

MANUSCRIPT RECEIVED AUGUST 18, 2009

MANUSCRIPT ACCEPTED JANUARY 30, 2010

MANUSCRIPT HANDLED BY DON BAKER